

Department of Physics and Astronomy

University of Heidelberg

Master thesis

in Physics

submitted by

Max Simon

born in Heilbad Heiligenstadt

December 2020

**On the Impact of Submesoscale Fronts on
Mesoscale Eddies and Biological Productivity
in the California Current System**

This Master thesis has been carried out by Max Simon

at the

Department of Environmental Systems Science, ETH Zurich

under the supervision of

Prof. Dr. Norbert Frank,

Prof. Dr. Nicolas Gruber

and Dr. Matthias Münnich

Abstract

Submesoscale motions are often not resolved in numerical models, although recent studies suggest that they interact with mesoscale processes. This might be particularly relevant for regions like the California Current System (CCS) where mesoscale processes redistribute nutrients and organic matter to offshore regions. In this study, the impact of submesoscale fronts on mesoscale eddies and biological productivity is examined by comparing two models of the CCS with different horizontal resolutions: a conventional (7.0 km) and a front-permitting resolution (2.8 km). A novel detection algorithm was developed which allows quantifying the area covered by submesoscale fronts. The algorithm reveals that fronts occur more often in anticyclones than in cyclones. This results in a weakening of the density anomaly associated with anticyclones by 40 % during winter for the increased resolution. Further, the energy cascade of mesoscale eddies is better resolved contributing to the seasonal evolution of eddy kinetic energy. Finally, the biological productive band at the coast broadens, presumably driven by enhanced lateral transport of nutrients. The results demonstrate that submesoscale and mesoscale motions are inextricably linked and that regional numerical models should aim to resolve submesoscale fronts for future studies.

Zusammenfassung

Numerische Modelle lösen submesoskalige Prozesse häufig nicht auf, obwohl gezeigt wurde, dass sie auch mesoskalige Prozesse beeinflussen. Dies ist besonders in Regionen wie dem *California Current System* (CCS) relevant, da dort mesoskalige Prozesse am Transport von Nährstoffen und organischem Material in küstenferne Regionen beteiligt sind. In dieser Arbeit wird der Einfluss von submesoskaligen Fronten auf mesoskalige Eddies und biologische Produktivität untersucht, indem zwei Modelle des CCS mit unterschiedlicher horizontaler Auflösung verglichen werden: eine konventionelle (7.0 km) und eine feine Auflösung (2.8 km). Zudem wurde ein Erkennungsalgorithmus für submesoskalige Fronten entwickelt, der deren eingenommene Fläche ermittelt. Der Algorithmus zeigt auf, dass Fronten häufiger in Anticyclonen als in Cyclonen auftreten. Dies führt in der feineren Auflösung zu einer Abschwächung der Dichteanomalie in Anticyclonen von 40 % im Winter. Zudem wird die Energiekaskade von mesoskaligen Eddies und damit auch die Saisonalität der *eddy kinetic energy* (EKE) besser aufgelöst. Außerdem verbreitert sich die biologisch produktive Zone an der Küste, vermutlich durch verstärkten lateralen Transport von Nährstoffen. Die Ergebnisse zeigen, wie eng submesoskalige und mesoskalige Prozesse miteinander verbunden sind und dass regionale numerische Modelle submesoskalige Fronten für kommende Studien auflösen sollten.

Contents

List of abbreviations	iv
1 Introduction	1
2 Data & Methods	6
2.1 Model Setup	6
2.2 Mesoscale Eddy Detection	8
2.3 Metrics of Mesoscale Eddy Characterization	9
2.4 Detection Algorithm for Submesoscale Fronts	10
2.5 Error Estimation	13
3 Results	14
3.1 Mesoscale Eddies	14
3.1.1 Evaluation of Detection Results	14
3.1.2 Seasonality of Eddy Strength	16
3.2 Submesoscale Fronts	21
3.2.1 Appearance	21
3.2.2 Submesoscale Front Detection	24
3.3 Biological Productivity	27
3.3.1 Revisiting the Impact of Mesoscale Eddies	27
3.3.2 NPP in MR and HR	29
4 Discussion & Outlook	32
Appendices	38
A Additional Figures	39
B Lists	49

List of abbreviations

- BEC** Biological Elemental Cycling module
- CC** California Current
- CCS** California Current System
- CUC** California Undercurrent
- EBUS** Eastern Boundary Upwelling System
- EKE** eddy kinetic energy
- HR** high-resolution model
- MLD** mixed layer depth
- MLE** mixed layer eddies
- MLI** mixed layer instabilities
- MR** mid-resolution model
- NPP** net primary production
- ROMS** Regional Ocean Modeling System
- SSH** sea surface height

1 Introduction

The California Current System (CCS) is a highly productive coastal region (Carr, 2001) that also drives productivity in the northeast Pacific Ocean (Frischknecht et al., 2018; Gruber et al., 2011; Nagai et al., 2015; Renault et al., 2016). Over the last years, various studies suggested that processes with scales of 0.1 km to 10 km - the so called *submesoscale* - could have significant impacts on upper ocean dynamics (Boccaletti et al., 2007; Capet et al., 2008a; Mahadevan, 2016; McWilliams, 2016, 2019; Sasaki et al., 2014; Schubert et al., 2020; Thomas et al., 2005) and biological productivity (Kessouri et al., 2020; Lapeyre et al., 2006; Lévy, Ferrari, et al., 2012; Lévy et al., 2018; Lévy et al., 2001; Mahadevan, 2016; Omand et al., 2015; Stukel et al., 2017). However, the question about consequences for a consideration in numerical models remains open (Fox-Kemper et al., 2019). Therefore, this study examines how submesoscale processes impact larger scales and how this alter biological productivity.

The CCS is located at the west coast of North America. In this study, the focus is on the central CCS which extends from Cape Mendocino at 40°N to Point Conception at 35°N (Checkley et al., 2009). During spring and summer, equatorward winds lead to offshore Ekman transport and upwelling of cold, nutrient-rich water at the coast which fuels biological productivity (Huyer, 1983). In addition, two large scale flows occur in the region. The California Current (CC) is part of the North Pacific Gyre and appears as a broad, equatorward flow with velocities of $\sim 0.1 \text{ m s}^{-1}$. It is accompanied by intense jets of $\sim 0.5 \text{ m s}^{-1}$ which are $\sim 75 \text{ km}$ wide (Huyer et al., 1991). The poleward California Undercurrent (CUC) develops in response to equatorward winds. It is located close to the coast at 100 m to 300 m depth (McCreary et al., 1987). Biological and physical processes are tightly coupled in the CCS (Bograd et al., 2001) and are subject to strong interannual variability driven but not limited by basin-scale effects (Frischknecht et al., 2015). As a representative of Eastern Boundary Upwelling Systems (EBUS), the CCS shares similarities in ocean dynamics and biological productivity with other EBUS (Chavez et al., 2009).

The highly dynamic regime in the CCS gives rise to mesoscale processes, i.e. mesoscale eddies (Kelly et al., 1998). Emerging from instabilities in large scale currents, these coherent vortices have radii of 35 km to 100 km (first Rossby radius of deformation) and lifetimes of up to several months (Kurian et al., 2011). Mesoscale eddies are vertically hydrostatic and have a geostrophic horizontal flow, that is a counter-clockwise rotation of cyclones around a positive density anomaly in the Northern Hemisphere (anticyclones clockwise around a negative density anomaly) (McWilliams, 2008). Due to the vertical displacement of isopycnals, mesoscale eddies are also associated with an anomaly in sea surface height (SSH) that is negative for cyclones and positive for anticyclones. This allows for tracking of mesoscale eddies with satellites (Chelton, Schlax, et al., 2011; Ducet et al., 2000).

Mesoscale eddies impact biological productivity in several ways. They stir surrounding waters (Chelton, Gaube, et al., 2011; Rossi et al., 2008), trap fluids present during formation and thereby transport biogeochemical properties to distinct regimes (Chelton, Gaube, et al., 2011; Flierl, 1981; Nagai et al., 2015). In addition to lateral transport mechanisms, the vertical displacement of isopycnals impacts biological productivity. The displacement allows for adiabatic fluxes (along isopycnals) of biogeochemical tracers in to or out of the euphotic zone where they can fuel productivity (Falkowski et al., 1991; Freilich et al., 2019). Further, the displacement also changes the mixed layer depth (MLD) which is decreased for cyclones and increased for anticyclones. Thereby, the light exposure time of phytoplankton in light limited regimes is affected (McGillicuddy, 2016). Moreover, vertical transport of nutrients or biomass can be induced by surface stress (interaction with wind) (Gaube et al., 2015; McGillicuddy et al., 2008; Stern, 1965) or vortex deformations (interaction with other eddies or currents) (Martin et al., 2001). All these effects have been extensively investigated in observations (Friedrichs et al., 2009; Kahru et al., 2009) and numerical models (Frischknecht et al., 2018; McGillicuddy, 2016; Nagai et al., 2015).

In contrast, submesoscale motions are often not resolved in numerical models and less is known about their interaction with other scales and processes. The submesoscale lies between the mesoscale (dominated by rotation of the earth) and vertical turbulent mixing. It comprises spatial scales of 0.1 km to 10 km and temporal scales of days to weeks, which makes observations and numerical modelling challenging (Thomas et al., 2008). A lot of processes fall into the submesoscale (e.g. subsurface coherent vortices (McWilliams, 1985) or currents in the deep sea (Vic et al., 2018)),

but the focus of this study is on submesoscale fronts in the upper ocean and associated processes.

In the upper ocean, submesoscale fronts emerge at horizontal density gradients and are powered by atmospheric forcing and mesoscale strain (Thomas et al., 2008). Further, they can be intensified by Ekman transport induced by down-front winds (Thomas et al., 2005). They appear as transitory fronts of strong vertical velocity ($\sim 10^{-4} \text{ m s}^{-1}$, always up- and downwelling paired), are $\sim 10 \text{ km}$ wide and cover large parts of the upper ocean (Capet et al., 2008b). Their penetration depth is modulated by the MLD, thus they are strongest in winter (Callies et al., 2015; Mensa et al., 2013). An illustrative description of the physical processes leading to the formation of fronts - also called *frontogenesis* - can be found in Mahadevan (2016). Because the submesoscale is close to the resolution limit of current numerical models,

H1: we hypothesize that submesoscale frontogenesis is better resolved with higher horizontal resolution.

Submesoscale fronts are believed to impact the mesoscale. On the one hand, instabilities, also called mixed layer instabilities (MLI), can detach as mixed layer eddies (MLE) from frontal regions. The horizontal scale of MLE can be as small as $\sim 5 \text{ km}$ but they grow with time (Boccaletti et al., 2007). MLE restratify the mixed layer by overturning isopycnals from vertical to horizontal (Fox-Kemper et al., 2008; Lévy, Ferrari, et al., 2012; Whitt et al., 2017). Further, small eddies like MLE can be absorbed by mesoscale eddies and thus increases the kinetic energy of the merged eddy. Thereby, kinetic energy is transported from smaller to larger scales which is called *inverse energy cascade* (Sasaki et al., 2014; Schubert et al., 2020). On the other hand, symmetric instabilities in frontal regions dissipate kinetic energy and thereby drive a forward energy cascade from mesoscale to turbulent mixing (D’Asaro et al., 2011; Schubert et al., 2020).

The question arises if submesoscale fronts have to be considered in numerical models, despite the increased computational resources this requires. Capet et al. (2008a) were one of the first to address this question in the context of the CCS. They compared numerical models of an idealized CCS with different horizontal resolutions (down to 750 m) and investigated the dynamics at submesoscale fronts (Capet et al., 2008b) as well as the corresponding energy cascade (Capet et al., 2008c). In particular, they determined the length scale at which the energy flux changes sign (from inverse cascade to forward cascade) to be $\sim 35 \text{ km}$ (Capet et al., 2008c) which is much smaller than estimates from altimetry data of $\sim 100 \text{ km}$ (Tulloch et al., 2011).

This scale is impacted by eddies with a diameter as small as ~ 17 km (Schubert et al., 2020, Appendix B) which is close to the length scale of MLE. Recently, Schubert et al. (2020) confirmed that MLE strongly support the inverse energy cascade and that kinetic energy at mesoscale is reduced by up to 20 % when submesoscale motions are not resolved. However, the impact on single eddies remains unclear.

There are only few studies on how mesoscale eddy properties change when submesoscale fronts are resolved. In general, anticyclonic vorticity facilitate submesoscale instabilities (Haine et al., 1998; McWilliams et al., 2004; Thomas et al., 2013). This was observed for an idealized setup by Brannigan et al. (2017) who found instabilities to grow faster and at coarser resolutions in anticyclones than in cyclones. Furthermore, Schubert et al. (2019) compared numerical models of the Agulhas system with different horizontal resolutions and found that especially cyclones with a large amplitude in their SSH anomaly are better resolved in the high-resolution model. In this study, the focus is on the density anomaly of mesoscale eddies which is linked to the SSH anomaly. It describes the vertical displacement of isopycnals in the eddy core and thereby impacts biological properties. Following the findings of Schubert et al. (2019),

H2: we hypothesize that the resolution of submesoscale fronts leads to a strengthening of the density anomaly in cyclones whereas it remains unchanged for anticyclones.

The question how submesoscale fronts impact biological productivity is a much debated issue. On the one hand, the strong vertical velocities associated with submesoscale fronts can enhance the vertical transport of nutrients and organic matter with consequences for productivity and diversity (Lévy et al., 2018; Whitt et al., 2019). On the other hand, Lévy et al. (2018) concluded that their impact on nutrient supply to the euphotic zone is limited. The reason is that the fronts are bound to the MLD and that their seasonality is out of phase with the biological productive season in summer. However, they point out that restratification induced by MLE can impact productivity in light limited regimes (i.e. spring blooms) and that submesoscale dynamics might affect biodiversity, community structure and patchiness (Lévy et al., 2018). Nevertheless, resolving submesoscale processes can alter biological productivity indirectly, e.g. due to changes in the mean circulation (Lévy, Iovino, et al., 2012). Further, mesoscale processes which transport nutrients and organic matter, can be impacted as well. This was observed recently by Kessouri et al. (2020). They compared nutrient fluxes and biological productivity in the

CCS between models with 4 km and 1 km horizontal resolution and found that eddy quenching (an eddy-induced reduction of primary productivity at the coast, see chapter 3.3.1) is intensified in the high-resolution model. These findings and the changes induced by an increase of horizontal resolution are revisited in this study.

H3: We hypothesize that the biological productive band at the coast is broadened for an increased horizontal resolution.

The study is based on the comparison of two numerical models of the CCS: a mid-resolution (conventional) model with 7.0 km horizontal resolution and a high-resolution (front-permitting) model with 2.8 km horizontal resolution (see chapter 2.1). First, mesoscale eddies are identified using a SSH-based detection algorithm (see chapter 2.2) and compared between the two models in chapter 3.1. The presence and characteristics of submesoscale fronts are examined in chapter 3.2. To this end, a novel detection algorithm was developed which is described in detail in chapter 2.4. Thereafter, the differences between the two models regarding biological productivity, i.e. net primary production (NPP), are explored in chapter 3.3. In chapter 4 the results are gathered and implications are discussed.

2 Data & Methods

2.1 Model Setup

The data for this study was obtained with the Regional Ocean Modeling System (ROMS) which solves the three-dimensional primitive equations (Shchepetkin et al., 2005). The model uses curvilinear horizontal coordinates (see below) and terrain-following vertical coordinates with 64 layers (Song et al., 1994) which allows for a high resolution in the ocean surface layer. For a better representation of vertical velocities, the WENO numerical scheme is used (Shu, 1998; Vandemeulebrouck et al., 2020). Vertical mixing is parameterized by the commonly used KPP scheme for boundary layers (Large et al., 1994). For biochemistry, the Biological Elemental Cycling module (BEC) (Moore et al., 2013) is coupled to ROMS. This biogeochemical-ecological model involves different limiting nutrients, different phytoplankton functional types and the explicit cycling of carbon which enables more realistic productivity estimates in the considered domain (Frischknecht et al., 2017). The model parameters are the same as in Frischknecht et al. (2018), with the exception of the atmospheric forcing for which the ERA5 reanalysis dataset (Hersbach et al., 2020) is used.

In this study, only the central part of the CCS is analysed (grey area in Figure 2.1). The region within 200 km off the coast is referred to as *nearshore*, the region between 200 km and 800 km as *offshore*. The two models were run for five years with a climatological normal year forcing (based on year 1979). Only the last three years are considered for the analysis (see chapter 3.3.2 for the reason). The data is saved as bidaily averages.

Mid-resolution model

The horizontal grid used for the mid-resolution model (MR) is a telescopic grid (Bentsen et al., 1999) with poles at $41.5^{\circ}\text{N}, -114.0^{\circ}\text{E}$ and $-10.0^{\circ}\text{N}, 9.0^{\circ}\text{E}$ (see Figure 2.1). The grid has been used in previous studies on the CCS (Frischknecht et al., 2018; Frischknecht et al., 2017) because it benefits from a high resolution at the coast but still captures basin-scale effects. In addition, it shifts the error-prone, open lateral boundary far from the analysis region. The mean resolution of the subdomain used for analyses is 7.0 km (ranging from 4.6 km at the coast to 10.6 km offshore), the nominal resolution is 10 km^1 .

The initial conditions for MR are based on a spin-up of 20 years with a repeating forcing of year 1979 (first 10 years physics only, afterwards with BEC, unpublished work). A timestep of 600 s was used for this resolution.

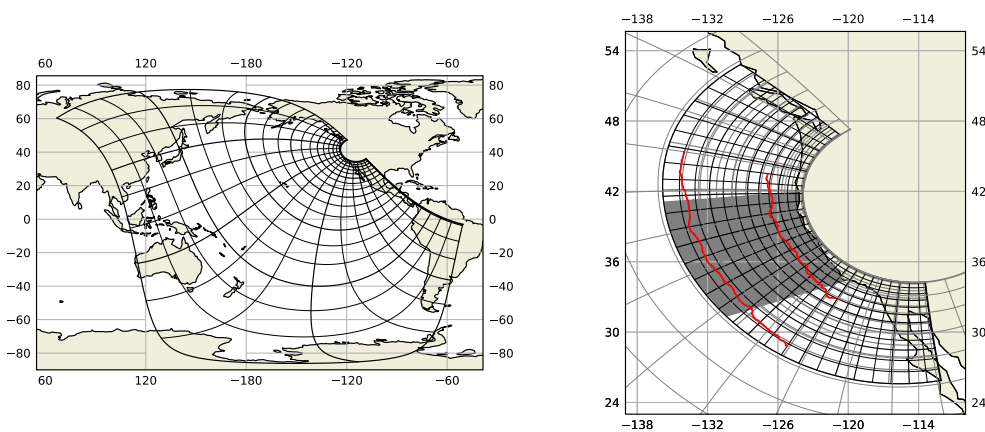


Figure 2.1: **Horizontal grids** for MR (left) and HR (right). Red lines denote 200 km and 800 km distance to coast. The gray area is the analysis domain.

High-resolution model

The horizontal grid used in the high-resolution model (HR) is also telescopic with the same poles as in MR. The horizontal resolution is increased by a factor of 2.5 to a mean resolution of 2.8 km (ranging from 1.8 km to 4.2 km) resulting in a nominal resolution of 5 km^1 .

¹The nominal horizontal resolution was calculated according to CMIP6 global attribute standards, see *CMIP6 Global Attributes, DRS, Filenames, Directory Structure, and CV's; Appendix 2* [website], <https://goo.gl/v1drZl> (accessed 17.11.2020, version 6.2.7).

In contrast to MR, HR is not integrated on the whole basin. Instead, the grid is clipped at ~ 1000 km off the coast (see Figure 2.1) and the results of MR are used as lateral boundary conditions. The initial conditions and the atmospheric forcing are the same as for MR (interpolated to HR grid). The timestep is reduced to 200 s.

2.2 Mesoscale Eddy Detection

Mesoscale eddies are detected using the algorithm of Faghmous et al. (2015) with adaptations for curvilinear grids implemented by Lovecchio et al. (2018). The algorithm defines an eddy as the largest closed contour of SSH anomaly around a single local extreme (minimum for cyclones, maximum for anticyclones). In a first step, local extremes are identified by comparing each pixel to its 5x5 neighborhood. Afterwards, the eddy extent is iteratively constructed around each extreme. At each iteration, neighbouring pixels with a SSH value above (or below) a threshold are assigned to the eddy and the threshold is increased (or decreased). The threshold starts from the extreme itself. As soon as the eddy comprises another extreme, the iteration stops and the previous iteration result is used as eddy extent (Faghmous et al., 2015, see their Figure 1.2). In this study, the threshold was changed by 5 cm at each iteration.

After eddies have been detected in each frame, a tracking algorithm developed by Chelton, Schlax, et al. (2011) assemble the instances to tracks. The algorithm matches an eddy at time t to an eddy at $t - 1$ if it is within a given radius of the previous detection. The radius is based on the propagation speed. In addition, the amplitude and size of the two instances have to be similar, meaning that they do not change more than by a factor of 0.25 to 2.75 between $t - 1$ and t . If no matching eddy was found in t , a *fake eddy* with the same size and amplitude as in $t - 1$ is placed along the eddy trajectory in t (based on the propagation speed from $t - 1$). The fake eddy can be matched in the following time step. This allows missing detections in tracks. The maximum number of consecutive fake eddies can be specified as a parameter (Faghmous et al., 2015, see their Figure 2). For this study, the number of consecutive fake eddies is set to 1 which corresponds to 2 d.

As proposed by Faghmous et al. (2015), the tracks are filtered based on their lifetime. Hence, only eddies belonging to tracks with a lifetime of more than 4 d (corresponding to 2 frames) are considered in this study.

2.3 Metrics of Mesoscale Eddy Characterization

The radius of an eddy r_e is defined as the radius of a circle with the same area as the eddy and is given as

$$r_e = \sqrt{\frac{A_e}{\pi}} \quad (2.1)$$

with A_e being the area of the eddy. It is commonly used (e.g. in Chelton, Schlax, et al. (2011) and Kurian et al. (2011)) because it is comparable to the Rossby deformation radius.

Eddies are associated with temperature and density anomalies. The anomaly of an observable X is given as $X'(t) = X(t) - \bar{X}(t)$ with \bar{X} being the mean state. For a characterization of eddies, \bar{X} should average out all eddy-induced variability but keep variability of larger scales (e.g. seasonal cycle or large-scale gradients). In this study, $\bar{X}(t)$ is approximated by averaging the climatology of X over 60 days around the day of year (DOY, given by t) with triangular weighting. The climatology at a given DOY is the average of all snapshots belonging to this DOY.

The eddy kinetic energy (EKE) is the kinetic energy of mesoscale horizontal motions (Rieck, 2019). It is given as

$$\text{EKE} = \frac{1}{2}u'v' = \frac{1}{2}(u - \bar{u})(v - \bar{v}) \quad (2.2)$$

with u, v being the surface horizontal velocity components and \bar{u}, \bar{v} their mean state.

Eddy composites are averages of a property (e.g. temperature anomalies) in the eddy impact region over many eddy instances. They can be thought of as a *mean eddy* (McGillicuddy, 2016). In order to calculate the composites, the eddy instances have to be resized to the same grid. This is achieved by applying the following steps to each eddy instance

1. determine radius r_e and center c_e of the eddy
2. get the data of the target property inside a bounding box of length $n*r_e$ centered at c_e
3. interpolate the extracted data to a fixed grid size of 50px \times 50px.

n determines the eddy impact area and is chosen to be $n = 4$ in this study. In order to perform a meaningful interpolation, only eddies with $r_e > 35$ km are considered for composites in this study.

2.4 Detection Algorithm for Submesoscale Fronts

Submesoscale fronts occur as elongated fronts of strong vertical velocities in the upper ocean (McWilliams, 2016). In the course of this study, a detection algorithm was developed which detects fronts in the vertical velocity field. It makes use of three characteristics of the fronts: (1) enhanced vertical velocity (up or down), (2) elongation and (3) consistency in depth. The algorithm consists of three steps which are defined below for the detection of upward fronts (for downward fronts only the sign in the thresholding step changes). The steps are also illustrated in Figure 2.2.

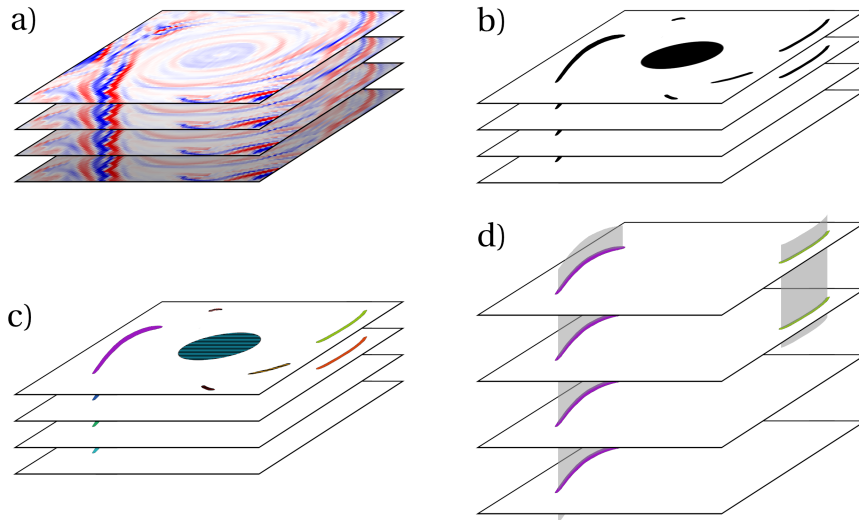


Figure 2.2: **Steps of submesoscale front detection algorithm.** (a): The 3D vertical velocity field used as input. (b): Pixels of strong vertical velocities are identified by applying an adaptive threshold $t_w(z)$ ($\Rightarrow P_{hvv}$). (c): The pixels are grouped by a 2D connected component analysis to distinct components ($\Rightarrow \tilde{C}$). Too small or circular components are dropped ($\Rightarrow C$). (d) The remaining components are combined vertically by a 3D connected component analysis to a set of possible fronts ($\Rightarrow \tilde{F}$). Only fronts that exceed several depth levels are kept ($\Rightarrow F$).

Step 1: A threshold $t_w(z)$ for the vertical velocity is calculated to obtain regions with strong vertical velocities. To this end, the vertical velocity field $w(x, y, z)$ is smoothed laterally (Gaussian filter with σ_{lat}) resulting in $w_{\text{smooth}}(x, y, z)$. $t_w(z)$ is then calculated as the lateral average of the absolute value of w_{smooth} :

$$t_w(z) = \langle |w_{\text{smooth}}(\cdot, \cdot, z)| \rangle. \quad (2.3)$$

Note, that $t_w(z)$ can be different for different depth levels. With $t_w(z)$ a set of pixels with enhanced vertical velocity can be defined for every depth level. This is given as

$$P_{\text{hvv}}(z) = \{p | p \in P(z), w(x_p, y_p, z) - w_{\text{smooth}}(x_p, y_p, z) \geq 2t_w(z)\} \quad (2.4)$$

with (x_p, y_p) being the location of the pixel p and $P(z)$ the set of all pixels at depth level z . For downward fronts, the set is given as

$$P_{\text{hvv}}(z) = \{p | p \in P(z), w(x_p, y_p, z) - w_{\text{smooth}}(x_p, y_p, z) \leq -2t_w(z)\}. \quad (2.5)$$

Step 2: A two-dimensional connected component analysis is carried out on $P_{\text{hvv}}(z)$ (more precisely on a boolean map where all pixels $\in P_{\text{hvv}}(z)$ are 1 and all others are 0). This transforms the pixel space into distinct components. The resulting components $\tilde{C}(z)$ are filtered by two criteria. The first criterion is that the number of pixels belonging to a component $c \in \tilde{C}$ (denoted as $\#c$) exceeds a minimum threshold of n_{comp} pixels. This removes very small components which are considered to be noise. The second criterion is that the ratio between $\#c$ and the area of the bounding box enclosing the component (denoted as $\text{bbox}(c)$) should be smaller than a threshold r_{comp} ($0 \leq r_{\text{comp}} \leq 1$). This criterion ensures that the components are elongated (a line has a very small ratio, a circle has a ratio of 0.79). The filtering of $\tilde{C}(z)$ results in

$$C(z) = \left\{ c | c \in \tilde{C}(z), \#c \geq n_{\text{comp}}, \frac{\#c}{\text{bbox}(c)} \leq r_{\text{comp}} \right\} \quad (2.6)$$

Step 3: The identified components are combined vertically. To this end, a set of pixels presumably associated with fronts is constructed:

$$P_{\text{front}} = \left\{ p | p \in \bigcup_{z \in \{0, \dots, Z\}} \bigcup_{c \in C(z)} c \right\} \quad (2.7)$$

Model	σ_{lat}	n_{comp}	r_{comp}	n_{depth}
MR	2	4	0.5	5
HR	2	10	0.5	5

Table 2.1: **Parameters for submesoscale front detection**

with Z being the maximum depth level. A three-dimensional connected component analysis is carried out on P_{front} (as described before) resulting in a set of possible fronts \tilde{F} . A front $f \in \tilde{F}$ is accepted as a front if its vertical extension (number of depth levels with non-zero components, denoted as $\#_z f$) exceeds a minimum threshold of n_{depth} depth levels. This criterion ensures consistency in depth. The final set of detected fronts F is then given as

$$F = \left\{ f \mid f \in \tilde{F}, \#_z f \geq n_{\text{depth}} \right\} \quad (2.8)$$

The optimal set of parameters was determined by visual inspection of the detection results. The chosen parameters used in this study can be found in Table 2.1. It turned out that σ_{lat} is the most important parameter. Because the thresholding step uses the deviation from w_{smooth} , σ_{lat} implicitly determines the width and number of detected fronts. This can be seen in Figure A.7 which shows detections for different values of σ_{lat} . The sensitivity to σ_{lat} is a strong limitation and future studies should seek a more robust thresholding. In contrast, the results seem to be less sensitive to the choice of n_{comp} and n_{depth} as small values for these thresholds are sufficient to filter out false detections. Also r_{comp} allows for a large margin because most features are strongly elongated and are clearly distinguishable from circular features.

Overall, the algorithm shows an acceptable performance. Fronts are detected in both models during winter (see Figure A.1 to A.3 for HR and Figure A.5 to A.6 for MR) and hardly any fronts are detected during summer (see Figure A.4). The number of fronts does not seem to be a meaningful metric, because the algorithm detects each upwelling- and downwelling component as a single front. Visual inspection confirms however, that the area covered by submesoscale fronts is captured quite well by the detection algorithm.

2.5 Error Estimation

The results of this study are based on detections of mesoscale eddies and submesoscale fronts. Unfortunately, the detection algorithms do not provide information about confidence of a detection. Therefore, the uncertainty Δx of a value x is approximated in this study by the interannual range of x , i.e. $\Delta x = \frac{1}{2}(\max_{\text{years}}(x) - \min_{\text{years}}(x))$. Although this approximation is convenient, it is likely to underestimate the true uncertainty because a normal year forcing is used in this study. Moreover, spatial and seasonal variability is not captured by this approach. Hence, the reported uncertainties have to be taken with caution.

3 Results

3.1 Mesoscale Eddies

3.1.1 Evaluation of Detection Results

The detection algorithm of Faghmous et al. (2015) detects $\sim 25\%$ more eddies in HR than in MR. During the three years of analysis, 24.9 ± 0.2 cyclones and 22.2 ± 0.2 anticyclones are detected in MR per day. On the other hand, 34.5 ± 0.3 cyclones and 29.7 ± 0.2 anticyclones are detected in HR per day. Both models show a slight increase in the number of detected eddies from March to October, but the ratio of cyclones to anticyclones is constant in the course of the year (1.14 ± 0.01 in MR, 1.18 ± 0.01 in HR). The ratio compares very well to ratios of 1.18 reported by Kurian et al. (2011, see their Figure 5) and 1.15 – 1.25 reported by Nagai et al. (2015), albeit they used a different detection algorithm. The number of detections is not directly comparable because the studies analysed a larger part of the CCS.

The increased number of detections in HR is caused by detection of more smaller eddies with a radius $r_e \leq 30$ km. This can be seen in the distribution of r_e which is shown in Figure 3.1. Only $(37.0 \pm 1.2)\%$ of all detected eddies in MR have a radius $r_e \leq 30$ km, whereas $(59.5 \pm 1.6)\%$ in HR fall in this category. For the range $30 \text{ km} \leq r_e < 100 \text{ km}$, the number of detections is very similar in MR and HR. Very large eddies with radius $r_e > 100$ km are less present in HR but are rare in both models. The number of detections decreases exponentially with increasing radius which is consistent with results from Kurian et al. (2011, see their Figure 5).

The detection algorithm defines eddies as closed contours in SSH around a single extremum (Faghmous et al., 2015). Hence, the algorithm is sensitive to the smoothness of the SSH field and thus to the horizontal resolution. To evaluate the impact of this effect, the SSH field of HR was interpolated to the grid of MR. As expected, the fraction of smaller eddies is reduced to $(42.6 \pm 1.0)\%$, but it is still higher than

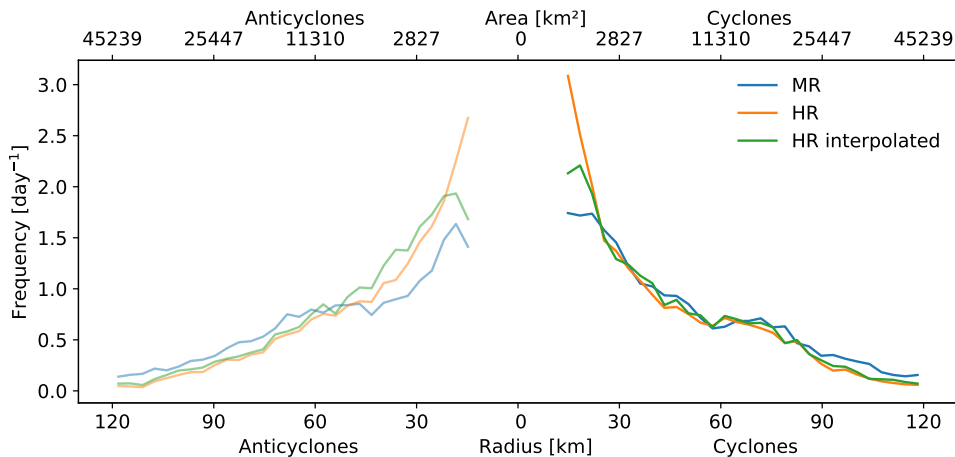


Figure 3.1: **Distribution of eddy radius.** The distribution is plotted to the right for cyclones and to the left for anticyclones.

for MR. This indicates that there are indeed more smaller eddies in HR than in MR and that it is not just caused by the sensitivity of the detection algorithm.

The radius of eddies increases with their distance to the coast (see Figure A.8). Within the first 250 km off the coast, the average radius increases by $\sim 60\%$ from 19 km (13 km) to 48 km (31 km) in MR (HR). Beyond 250 km, eddies grow slower and approach a radius of 63 km (48 km) around 800 km off the coast in MR (HR). This evolution has also been observed by Kurian et al. (2011, see their Figure 8).

Regarding the lifetime, cyclones are more stable than anticyclones, especially in HR. On the one hand, the average lifetime of cyclones (83 d in MR, 58 d in HR) is longer than the average lifetime of anticyclones (70 d in MR, 49 d in HR). Though, the values have high variance of $\sim 150\%$ as the lifetimes can reach from few days to several months. On the other hand, cyclonic dominance increases for long-lived eddies. More precisely, the ratio of cyclonic to anticyclonic tracks increases with an increasing threshold of minimum lifetime (see Figure 3.2). This is in accordance with results of Kurian et al. (2011, see their Figure 5). The effect is stronger in HR as the ratio is larger in HR for every minimum lifetime threshold. For a minimum lifetime of 90 d for example, there are 113 (115) cyclones and only 95 (83) anticyclones in MR (HR). Results regarding lifetime of eddies should be treated with caution, because the tracks are likely to be biased to short tracks. The reason is that missing detections or eddy interactions can lead to an early stopping of tracks and eventually a starting of new tracks. Nevertheless, a comparison of cyclones and anticyclones is valid as both are affected by this issue.

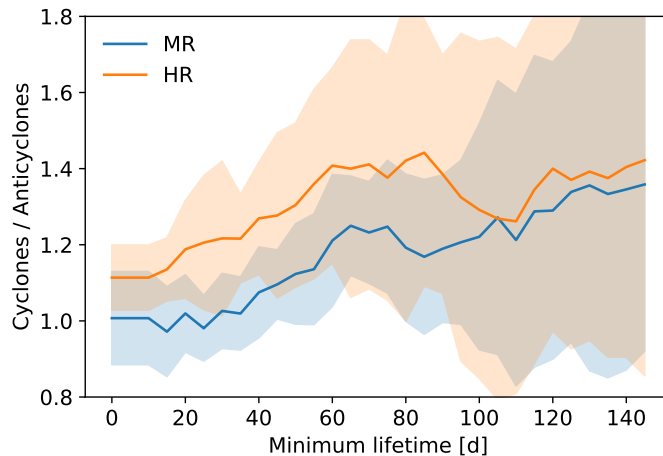


Figure 3.2: **Ratio of cyclonic to anticyclonic tracks.** The shaded area represents the interannual variability. The reason for the high variability is twofold: the number of tracks decreases with increasing threshold and the tracks had to be attributed to a single year although they can span two years.

3.1.2 Seasonality of Eddy Strength

The most energetic mesoscale eddies are formed nearshore during summer. This can be seen in Figure 3.3 which shows the EKE associated with cyclones and anticyclones. During summer and autumn, the eddies move offshore (westwards) and reach the offshore region in winter where most of the associated energy dissipates. This seasonality has been observed in various other studies as well (Chaigneau et al., 2009; Checkley et al., 2009; Kelly et al., 1998; Kurian et al., 2011). Compared to MR, the overall EKE (i.e. independent of eddy detections) increases by $(10.2 \pm 0.5) \%$ in HR with a maximum increase of $(14.9 \pm 1.0) \%$ during spring. This matches well to observations of Schubert et al. (2020) who observed a reduction of kinetic energy in the mesoscale by $\sim 20 \%$ when submesoscale motions are not resolved.

In the nearshore region, an outstanding difference between MR and HR is the enhanced activity of eddies in spring (see Figure 3.3). From March to June, the mean EKE of nearshore anticyclones is $(18.3 \pm 0.4) \times 10^{-3} \text{ m}^2 \text{ s}^{-2}$ in MR compared to $(26.2 \pm 0.4) \times 10^{-3} \text{ m}^2 \text{ s}^{-2}$ in HR. This matches to the increase of overall EKE during spring mentioned above. A reason for the increase could be a difference in the strength of the CUC, because the formation of nearshore eddies is strongly driven by vertical shear induced by the undercurrent (Checkley et al., 2009; Kurian et al., 2011). The strength of the CUC can be assessed by the horizontal velocity component u because the curvilinear gridlines of the model are approximately par-

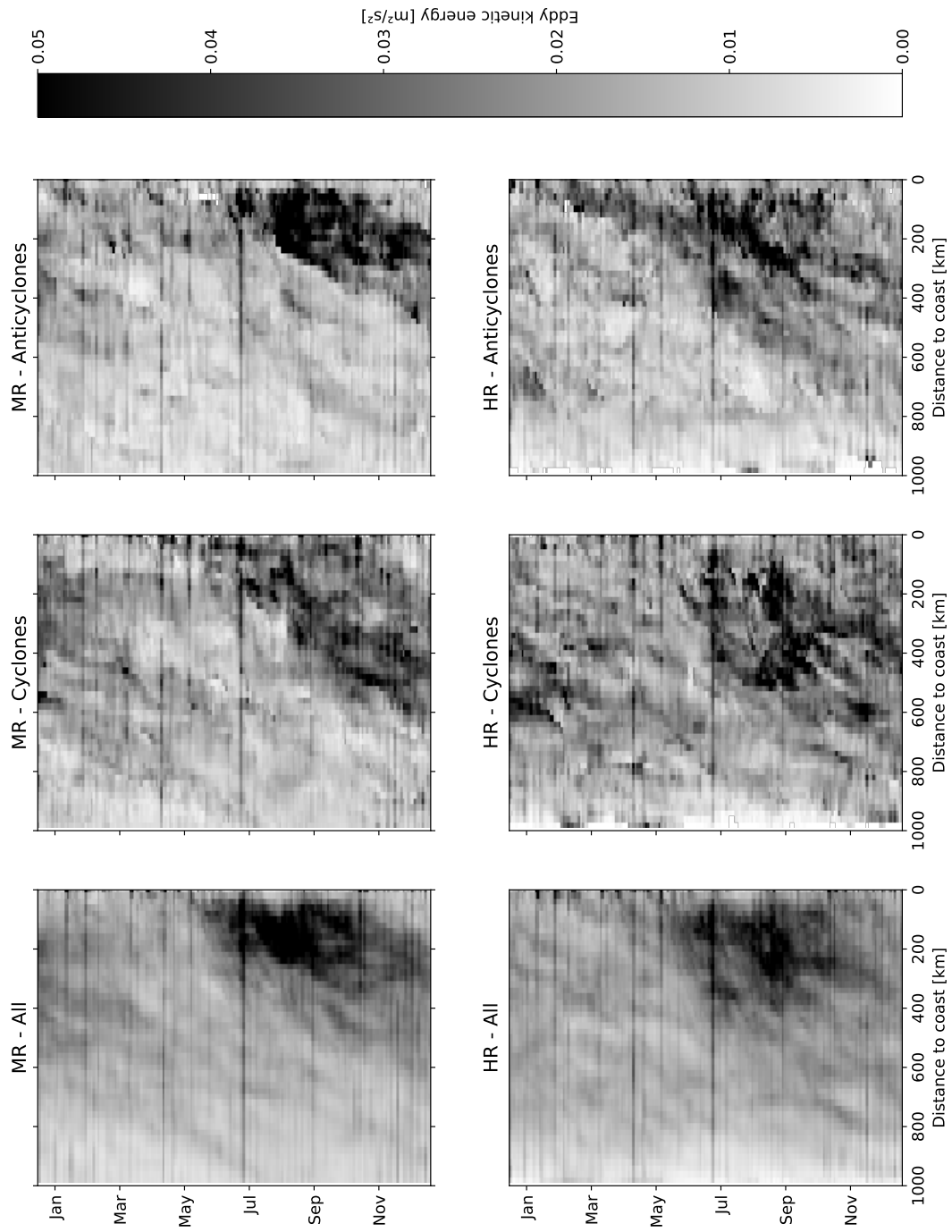


Figure 3.3: **Eddy Kinetic Energy** of MR (top) and HR (bottom). The EKE is shown for the whole domain (i.e. independent of eddy detections) left, for cyclones in the center and for anticyclones right.

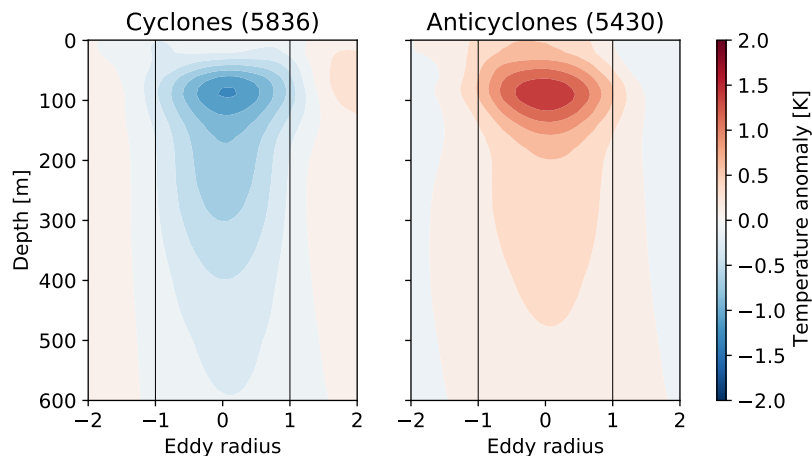


Figure 3.4: **Vertical structure of temperature anomaly.** The number of aggregated eddies is denoted in brackets.

allel to the coast (see chapter 2.1). From February to March, the CUC and the CC are stronger in HR than in MR (see Figure A.9). In contrast, both currents are of similar strength in HR and MR from June to August. The stronger CUC generates more shear which might be a reason for the enhanced eddy activity in early spring. An investigation of the exact reason for the different strength is out of the scope of this study. Nevertheless, it should be noted that both models differ from observations of Rudnick et al. (2017, see their Figure 4.2.3.1 to 4.2.3.4) or model results of Renault et al. (2020, see their Figure 20). Therefore, future studies should pay special attention to the tuning of the CUC strength.

Before the density anomaly is examined, the vertical structure of the anomalies in mesoscale eddies is briefly discussed. Figure 3.4 shows the vertical structure of the temperature anomaly in MR. It primarily follows the density anomaly, but Kurian et al. (2011) only report the temperature anomaly. The anomaly extends down to more than 500 m and has a maximum ~ 100 m. A similar depth of maximum anomaly was found by Kurian et al. (2011, see their Figure 16), though they report weaker anomalies (-0.78 K and 0.48 K compared to ~ -1.0 K and ~ 1.2 K in this study). This can be explained by the different definition of anomaly: Kurian et al. (2011) approximate the mean state as a spatial average over a box of $85\text{km} \times 85\text{km}$ around the eddy core. Considering the typical eddy size, this removes less of the eddy-induced variability from the mean state than the method applied in this study (see chapter 2.3).

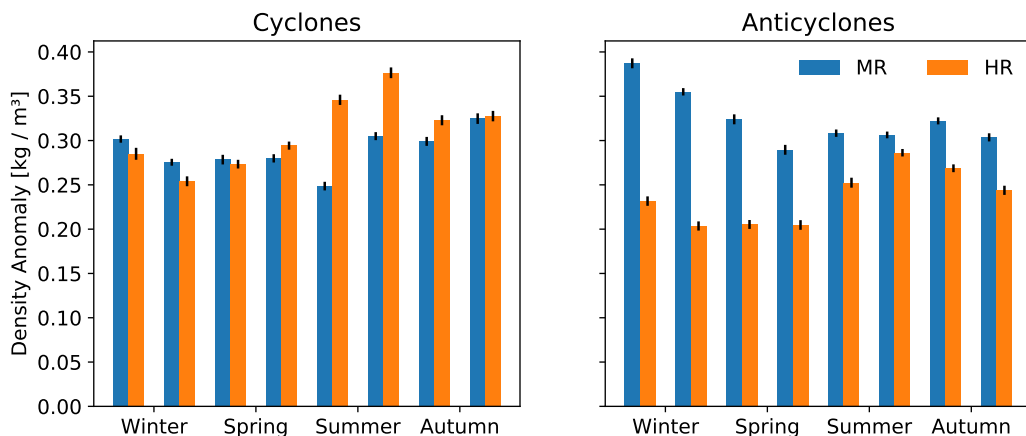


Figure 3.5: **Offshore density anomaly.** The black bars denote the interannual variability. Note, that the anomaly is negative in anticyclones.

Regarding the density anomaly, offshore cyclones exhibit a seasonality in HR which is not present in MR. The average anomaly between 80 m and 120 m (which includes the maximum) is shown in Figure 3.5. The anomaly in MR has little variance (values range from $25 \times 10^{-3} \text{ kg m}^{-3}$ to $32 \times 10^{-3} \text{ kg m}^{-3}$ without a trend). In contrast, the anomaly in HR increases systematically from $(25.4 \pm 0.6) \times 10^{-3} \text{ kg m}^{-3}$ in late winter to $(37.6 \pm 0.6) \times 10^{-3} \text{ kg m}^{-3}$ in late summer.

The effect is also visible in EKE associated with offshore cyclones. Figure 3.6 shows the relative increase in EKE from MR to HR: cyclones start to intensify in late spring and are $\sim 50\%$ more energetic during summer in HR than in MR. But even during winter the EKE is $\sim 20\%$ higher in HR. This is mainly driven by spontaneous (i.e. not related to eddies coming from nearshore) and localized boosts of the EKE (see e.g. at 400 km off the coast in March, Figure 3.3).

By contrast, the density anomaly of offshore anticyclones differ strongly between MR and HR. The difference is largest in winter where the anomaly drops from $(-37.1 \pm 0.6) \times 10^{-3} \text{ kg m}^{-3}$ in MR to $(-21.8 \pm 0.5) \times 10^{-3} \text{ kg m}^{-3}$ in HR (see Figure 3.5). This difference is much larger than the maximum difference observed for cyclones. As a result, the year-round density anomaly of anticyclones is smaller than for cyclones in HR, whereas it is larger than for cyclones in MR. Yet, the seasonality of anticyclones in HR is very similar to the seasonality of cyclones. Regarding the EKE associated with anticyclones, an intensification in late spring and early summer appears which is very similar to cyclones. However, EKE is hardly increased during winter which is in accordance with the described weakening (see Figure 3.6).

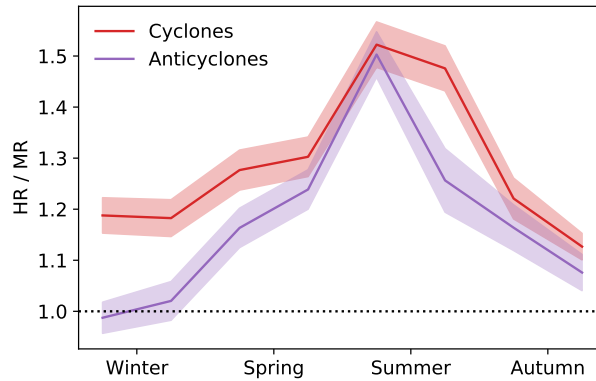


Figure 3.6: **Relative increase in offshore EKE.** The shaded area represents the interannual variability.

The presented findings do not depend on the exact choice of the depth range used for averaging the anomaly. This was tested by comparing the presented results for the range 80 m to 120 m depth to the range 25 m to 200 m depth. Although the absolute values change, the described trends are still present (see Figure A.10).

In summary, the properties of the detected eddies are consistent with previous studies of the CCS, e.g. Kurian et al. (2011). The increase in horizontal resolution leads to more smaller eddies ($r_e < 30$ km) and impacts the strength of eddies, nearshore and offshore. In the nearshore region, eddy activity is enhanced during spring which is probably related to a stronger CUC. In the offshore region, the density anomaly exhibits a seasonality in HR with a minimum during winter and a maximum during summer. Compared to MR, the anomaly of anticyclones is strongly damped in HR during winter and spring. This is accompanied with an increased ratio of cyclones to anticyclones and less stable anticyclonic tracks in HR.

3.2 Submesoscale Fronts

3.2.1 Appearance

During winter, large parts of the upper ocean are covered by submesoscale fronts. Compared to MR, the fronts clearly stand out in the vertical velocity field of HR (see snapshot in Figure 3.7 for HR and in Figure 3.8 for MR). The fronts are ~ 10 km wide, ~ 100 km long and occur always as pairs of upwelling and downwelling fronts. Often, several fronts can be found close to each other and they are collocated with lateral density gradients (see Figure 3.7). The associated vertical velocity is $\sim 5 \text{ m d}^{-1}$.

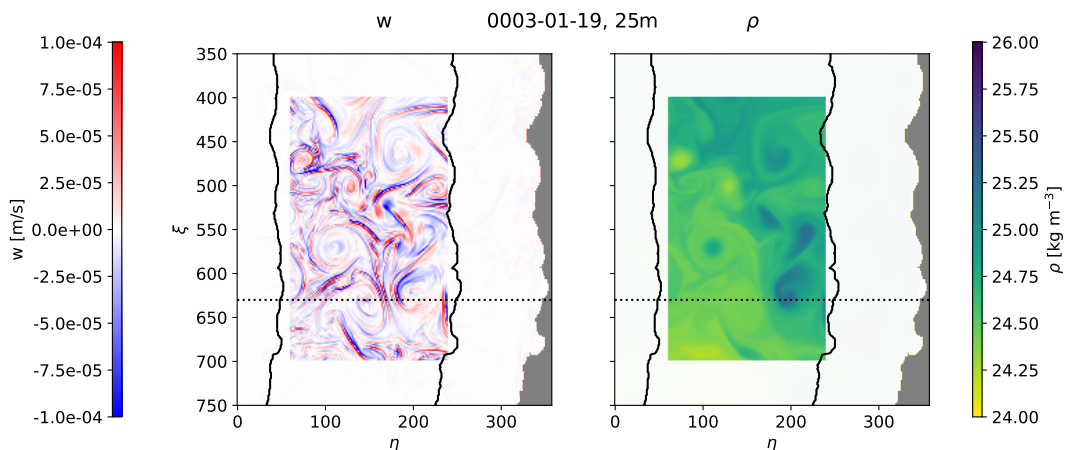


Figure 3.7: **Snapshot of submesoscale fronts in HR.** The snapshot is from mid January at 25m depth and shows the vertical velocity (right) and density (left). The domain is in grid coordinates η and ξ . The highlighted area is the area to which the detection algorithm is applied. Black solid lines represent 200 km and 800 km distance from coast. The dotted line is the location of the vertical section shown in Figure 3.9.

Submesoscale fronts are located at steep, outcropping isopycnals. This can be seen in Figure 3.9 which shows the vertical section of the vertical velocity in the offshore region. The vertical velocity is always negative (downward) at the dense side of the density front and positive at the less dense side which is characteristic for frontogenesis (Thomas et al., 2008). Further, it shows exemplarily that most of the fronts can be found between mesoscale eddies. This emphasizes the importance of eddy-induced strain for frontogenesis (Thomas et al., 2008).

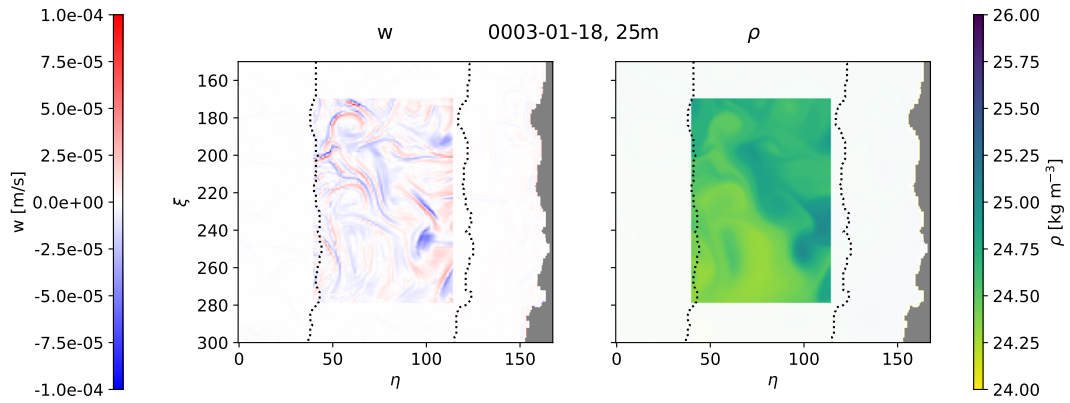


Figure 3.8: **Snapshot of submesoscale fronts in MR.** See Figure 3.7 for explanations.

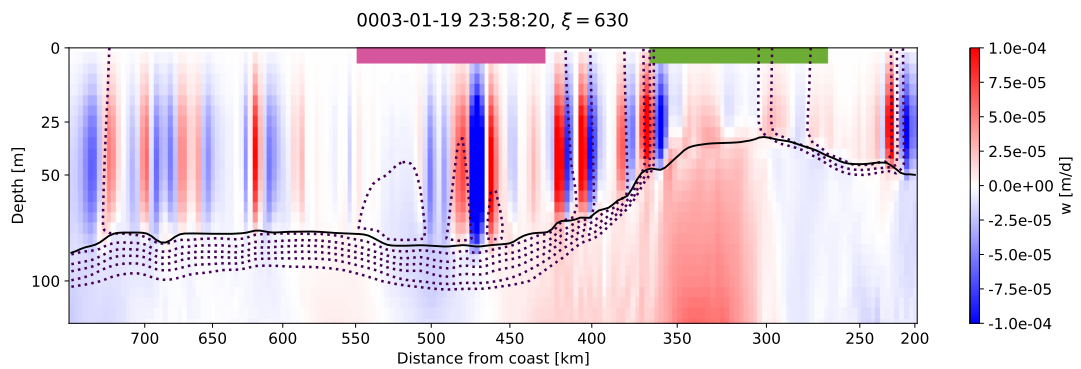


Figure 3.9: **Vertical section of submesoscale fronts.** The solid black line represents the MLD, dotted black lines show isopycnals. The green bars denote cyclones, pink bars anticyclones (positions from chapter 3.1.2).

Submesoscale fronts range from the surface to the base of the mixed layer and only few reach below it (see Figure 3.9). Therefore, their presence is strongly modulated by the seasonality of the MLD which is driven by atmospheric forcing. The MLD is deepest in winter and shallowest in summer (Callies et al., 2015). Also submesoscale fronts in MR and HR are strongest during winter, whereas only little activity is present during summer.

Submesoscale fronts disappear after several days either by getting weaker or due to MLI. The former happens when the front is not stabilized (e.g. by mesoscale strain or down front winds), because the vertical velocities act to dampen the density front (Thomas et al., 2008). On the other hand, MLI arise when the front is stabilized or further intensified (Boccaletti et al., 2007). Both mechanisms occur in HR which is shown in Figure 3.10. The front is stable in the first snapshot whereas 10 d later the front disperse to small MLE (visible in vorticity field).

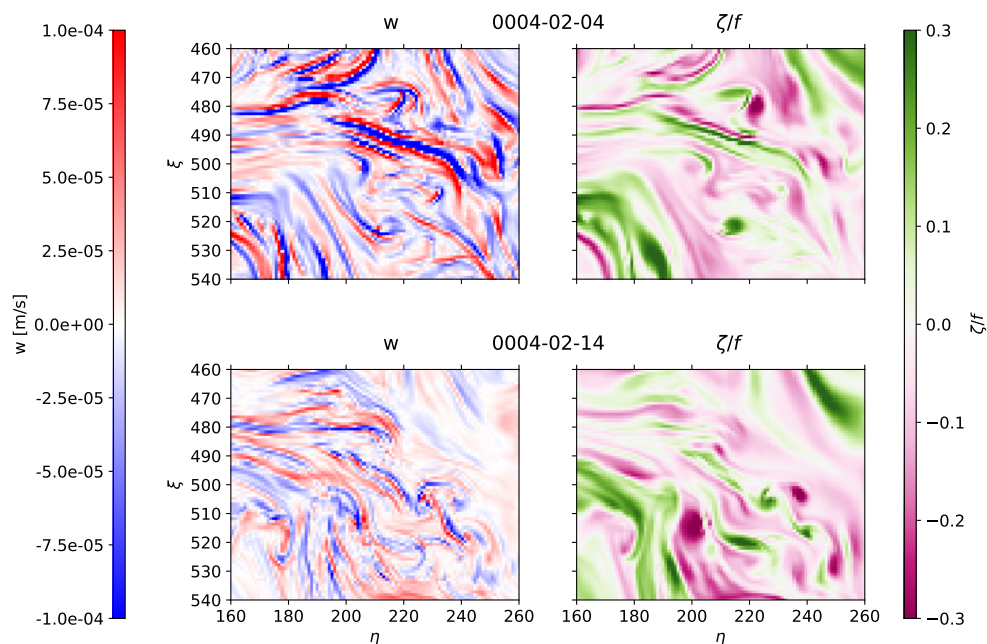


Figure 3.10: **Instabilities in submesoscale fronts.** Vertical velocity (left) and vorticity (normalized by f , right) at 25 m depth. The top row shows a snapshot from early February, the bottom row is ten days later.

3.2.2 Submesoscale Front Detection

In order to quantify the findings of chapter 3.2.1, a detection algorithm was developed to automatically detect submesoscale fronts in every snapshot. The algorithm makes use of three characteristics of submesoscale fronts: large vertical velocities, elongated spatial structure and consistency in depth. The method is described in detail in chapter 2.4.

The detection algorithm reveals, that submesoscale fronts cover larger parts of the offshore region in HR than in MR, especially at the base of the mixed layer. During winter, submesoscale fronts cover $(14.0 \pm 0.1) \%$ of the upper 30m of the considered domain in MR and $(16.2 \pm 0.1) \%$ in HR. The difference between MR and HR increases at greater depths. When considering the 10 m around the MLD (calculated for each day as domain average), only $(5.3 \pm 0.1) \%$ of the domain in MR is covered by submesoscale fronts whereas $(10.1 \pm 0.1) \%$ is covered in HR. The coverage is also visualized in Figure 3.11. The data shown in the plot also confirm the qualitatively observed modulation by the MLD as well as the seasonal cycle of submesoscale fronts. From these results, it can be concluded that submesoscale fronts are much better resolved in HR. Therefore, the following part refers only to HR.

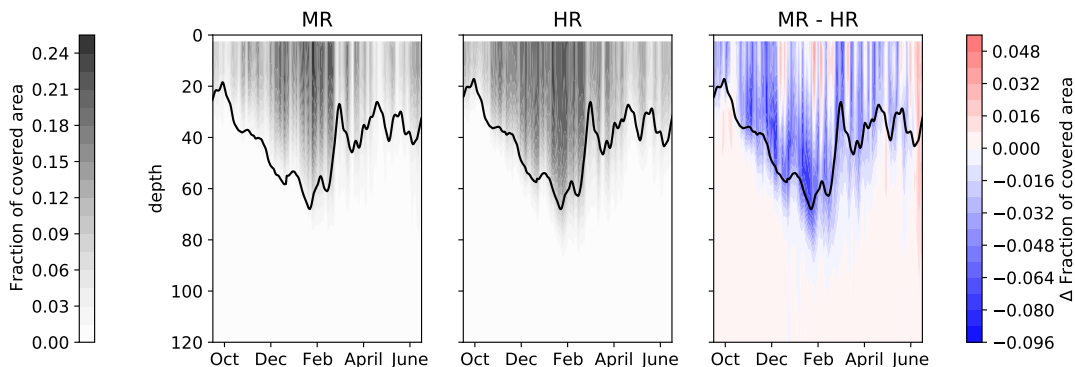


Figure 3.11: **Area covered by submesoscale fronts** relative to total area. MR is shown left, HR in the center. The difference MR - HR is shown right. The solid line denotes the average MLD

The detection algorithm reveals a slight asymmetry between upwelling and downwelling fronts. The area covered by upwelling fronts is on average $(3.1 \pm 0.6) \%$ larger than the area covered by downwelling fronts. Further, the average downwelling velocity $(-2.94 \pm 0.01) \text{ m d}^{-1}$ is $(8.9 \pm 0.3) \%$ larger than the upwelling velocity $(2.65 \pm 0.01) \text{ m d}^{-1}$. This asymmetry is indeed expected for submesoscale

frontogenesis (Mahadevan et al., 2006). The occurrence of the asymmetry in the detection results indicates that the algorithm is capable of detecting the fronts quite precisely.

Submesoscale fronts impact mesoscale anticyclones stronger than cyclones. Overall, fronts appear mainly outside of mesoscale eddies: during winter, $(75.1 \pm 1.4) \%$ of the area associated with submesoscale fronts is located outside of mesoscale eddies, albeit the eddies cover $(31.3 \pm 3.4) \%$ of the domain. The remaining area is distributed on mesoscale eddies with $(10.3 \pm 0.4) \%$ occurring in cyclones and $(14.5 \pm 0.4) \%$ in anticyclones. This difference is particularly interesting, because cyclones cover a majority of $(63.1 \pm 7.3) \%$ of the area associated with mesoscale eddies during this time. As a result, only $(8.3 \pm 0.5) \%$ of the area associated with cyclones intersect with submesoscale fronts whereas $(20.0 \pm 0.9) \%$ of the anticyclonic area do. Furthermore, submesoscale fronts occur in anticyclones not only at the eddy edge (as they do in cyclones) but also inside the eddy core. This can be seen in composites of the absolute vertical velocity in Figure 3.12. The composites are only based on mesoscale eddy detection and thus confirm the finding independently from the detection algorithm for submesoscale fronts.

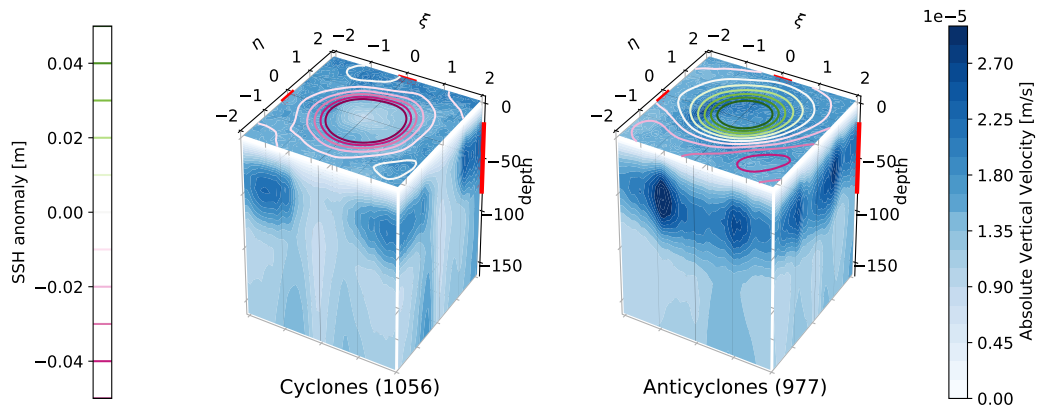


Figure 3.12: **Vertical velocity anomaly in HR.** Composite for cyclones is shown left and for anticyclones right. Only offshore eddies from January to March were considered. Contours on top represent SSH anomalies. The surfaces are averages of the perpendicular axes, the range for the averages are shown in red on the axes. The number of aggregated eddies is denoted in brackets.

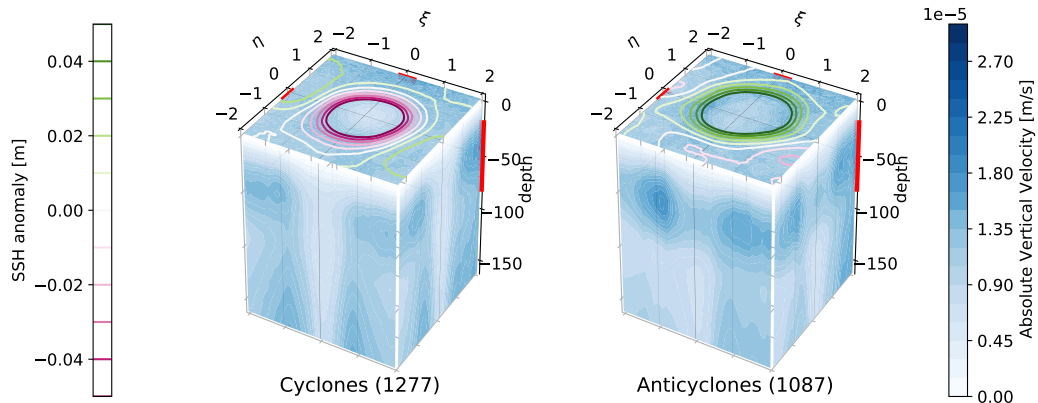


Figure 3.13: **Vertical velocity anomaly in MR.** See Figure 3.12 for explanations.

In contrast, the interaction of submesoscale fronts with mesoscale eddies, especially anticyclones, is much weaker in MR: only $(7.0 \pm 0.6)\%$ of cyclones and $(11.7 \pm 0.5)\%$ of anticyclones are covered by submesoscale fronts. Accordingly, the vertical velocities inside the eddies are also less affected (see Figure 3.13 in comparison to Figure 3.12).

In summary, the process of submesoscale frontogenesis is much better resolved in HR than in MR. The appearance in HR matches well to theoretical expectations (see chapter 1) or observations from previous studies (e.g. Capet et al. (2008b)). Even MLE can be observed in HR, albeit this is very close to the resolution limit. Furthermore, results of the detection algorithm confirm that fronts are modulated by the MLD and that they are most active during winter. In addition, a strong intersection of submesoscale fronts and mesoscale eddies can be detected in HR. At this, especially anticyclones are affected. This asymmetry is discussed in detail in chapter 4.

3.3 Biological Productivity

3.3.1 Revisiting the Impact of Mesoscale Eddies

McGillicuddy (2016) identified two important mesoscale processes that impact the productivity in an EBUS: lateral export of biomass by eddy stirring (described by Rossi et al. (2008) for Canary EBUS) and the subduction of upwelled nutrients (also called eddy quenching, described by Gruber et al. (2011) for California EBUS). Both processes are briefly discussed with data from MR.

Eddy composites of surface chlorophyll anomalies indicate that mesoscale eddies trap water masses and stir surrounding water. The composites are shown in Figure 3.14 and are very similar to observations from Gaube et al. (2014, see their Figure 9d). A decomposition reveals a strong monopole contribution and a dipole-like residual. The monopole can be a result of eddy pumping or trapping (Gaube et al., 2014). Because the CC flows southward and upwelling of nutrients is strongest close to the coast, cyclones trap in general nutrient rich water whereas anticyclones trap nutrient depleted water (Nagai et al., 2015). This matches the sign of the observed monopole contribution in the surface chlorophyll anomaly. Hence, the occurrence of trapping can be verified. But in contrast to Gaube et al. (2014), there is no indication for eddy pumping which would appear as an intensification of the anomaly during the first days of an eddy track. However, this finding strongly relies on the tracking algorithm (see chapter 3.1.2) and the authors note that the trend is not significant in their results either. The fact that stirring takes place can be seen in the dipole structure of the residual. The structure reflects the theoretical imprint of a westward travelling vortex in a tracer field with an east-to-west gradient (Chelton, Gaube, et al., 2011, see their Figure 3). In the case of the CCS, this gradient is produced by coastal upwelling.

Mesoscale eddies induce to a subduction of nutrients to an intermediate layer (~ 100 m) at which the nutrients are exported offshore. This effectively removes nutrients from the upwelling cycle and leads to a reduction of productivity at the coast in the long run (Gruber et al., 2011). Gruber et al. (2011) visualize the process using the eddy-induced nitrate flux \mathbf{j}_e which is given as

$$\mathbf{j}_e = \text{TN}'\mathbf{u}' = (\text{TN} - \overline{\text{TN}})(\mathbf{u} - \bar{\mathbf{u}}) \quad (3.1)$$

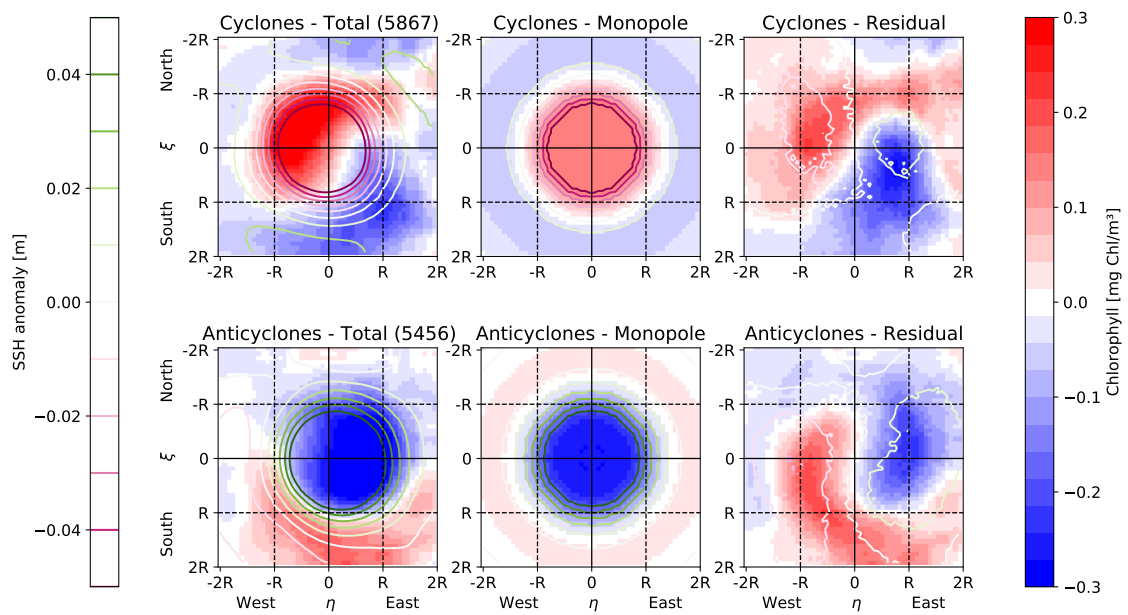


Figure 3.14: **Average surface CHL anomaly.** The total averaged CHL anomaly (left) was decomposed into a monopole by a radial mean (center) and a residual (right). The top row corresponds to cyclones, the bottom row to anticyclones. The contours represent SSH anomalies. The number of aggregated eddies is denoted in brackets.

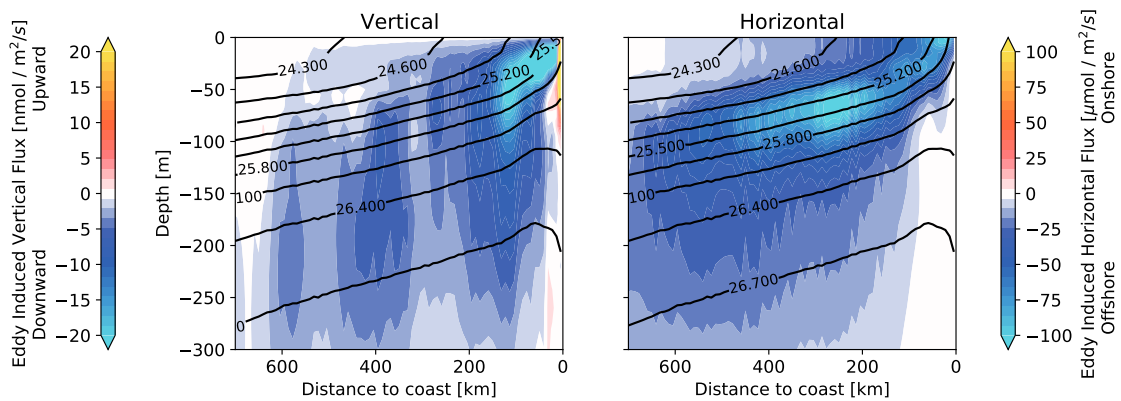


Figure 3.15: **Eddy-induced total nitrate flux.** The vertical component is shown left and the horizontal component right. Black lines denote isopycnals. Note the different order of magnitude and different color scale for the two components.

where TN is the total nitrogen and \mathbf{u} the velocity. The vertical and horizontal (perpendicular to the coastline) component of \mathbf{j}_e are shown in Figure 3.15. The components compare very well to the flux observed by Gruber et al. (2011, see their Figure 4), both in magnitude and location of up- and downwelling zones. The flux observed in this study omits a horizontal transport close to the surface and the upwelling region at the coast is slightly tighter. However, these differences do not impact the mechanism itself.

3.3.2 NPP in MR and HR

Biological productivity is highest at the coast and decreases continuously with distance to coast in both models (see Figure 3.16). The reason for this is that Ekman induced upwelling of nutrients fuels productivity at the coast from where nutrients and organic matter are transported offshore by mesoscale processes (Nagai et al., 2015). Compared to satellite observations (see Figure 3.16) and comparable numerical models (e.g. Deutsch et al. (2020, see their Figure 5)) both, MR and HR, overestimate NPP at the coast. This is probably related to a bad tuning of the model parameters to the new atmospheric forcing (see chapter 2.1, internal communication). However, conclusions are mainly drawn from the difference between MR and HR which should be less affected than the absolute values.

Compared to MR, NPP is reduced in HR by $(3.8 \pm 1.3)\%$ in the nearshore region and by $(11.0 \pm 1.7)\%$ within 50km off the coast (see Figure 3.17). The temporal

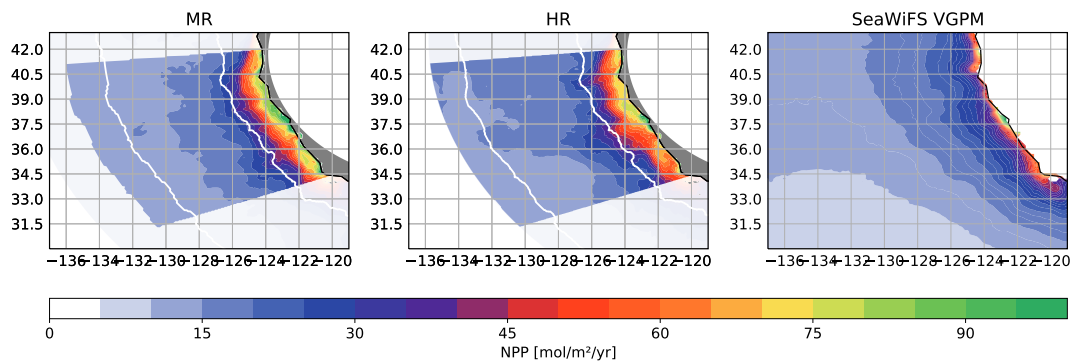


Figure 3.16: **Spatial distribution of NPP** in MR (left) and HR (center). NPP was integrated vertically and averaged over integration time. White lines denote 200km and 800km distance to coast. NPP derived from SeaWiFS data (1998-2007) using VGPM algorithm (Behrenfeld et al., 1997) is shown right.

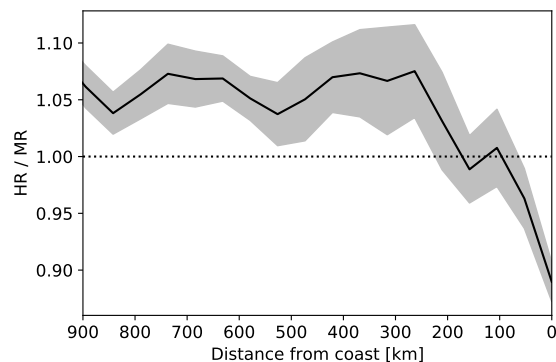


Figure 3.17: **Relative change of NPP with distance from coast.** The shaded region represents the interannual variability.

and spatial distribution of NPP is shown in Figure 3.18. The maximum difference between MR and HR appears in August, but the reduction starts already in April. This is similar to results of Kessouri et al. (2020) who compare two models of the CCS with horizontal resolutions of 4 km and 1 km. They also observe a reduction of NPP in the high-resolution model by up to 10% within 200 km off the coast and a maximum of the reduction in August. However, the reduction starts about a month later than observed in this study. Possible reasons for this delay are discussed in chapter 4.

In the offshore region, NPP is increased in HR by $(6.0 \pm 0.9)\%$ (see Figure 3.17). During spring, when offshore productivity is highest in both models, the difference

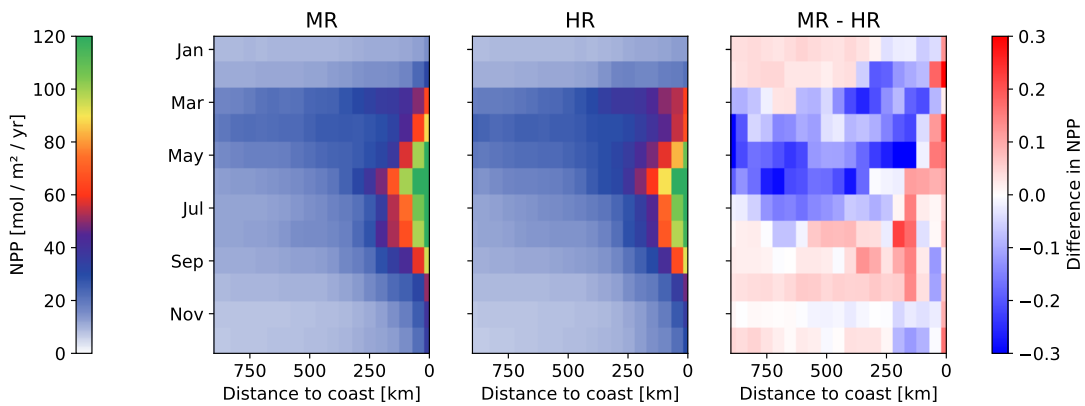


Figure 3.18: **Hovmöller diagram of NPP** for MR (left) and HR (right). The relative difference $(MR - HR)/MR$ is shown (right).

increases to $(14.4 \pm 2.0)\%$. Contrary to this, Kessouri et al. (2020) observe a year-round offshore increase in NPP with a maximum increase in late spring (see their Figure 6). This discrepancy is discussed in detail in chapter 4.

The observed differences in NPP between MR and HR have not converged and are still drifting at the end of integration. This can be seen in Figure A.11 which shows the difference in NPP for the nearshore and offshore region as a function of integration time. The increase in offshore NPP stabilizes after two years. This is the reason why the first two years were excluded from the analyses. However, the reduction of nearshore NPP strengthens throughout the integration time. Because the reduction is related to transport processes and redistribution of nutrients, this can also impact offshore productivity over time. Hence, it is very likely that the distribution of NPP in HR is not fully captured within the short integration time.

4 Discussion & Outlook

The study addressed the impact of submesoscale fronts on mesoscale eddies and biological productivity. To this end, two models of the CCS with different horizontal resolutions were compared, a conventional and a front-permitting resolution. First, effects on mesoscale eddies were examined by analysing the properties and strength of eddies (chapter 3.1). Afterwards, submesoscale fronts were characterized and analyzed for their interaction with mesoscale eddies. This was done using a novel detection algorithm for submesoscale fronts in the vertical velocity field (chapter 3.2). Finally, the lateral distribution of biological productivity was compared between the two models (chapter 3.3). In the following, the results are discussed with respect to the initial hypotheses.

With respect to hypothesis H1, it was found that submesoscale frontogenesis is much better resolved in HR than in MR. In HR, submesoscale fronts are ubiquitous during winter and spring, cover large parts of the upper ocean and shape the vertical velocity structure in the mixed layer. Important characteristics of frontogenesis, e.g. the seasonality, penetration depth or asymmetry of up- and downwelling, are confirmed by the detection algorithm for submesoscale fronts. This can also be understood as a validation for the algorithm.

The increase in resolution leads to a reduction of NPP in the nearshore region by $\sim 4\%$. Because mesoscale eddies are more energetic in HR, they are more effective in trapping water masses and hence exporting nutrients and organic matter to offshore regions. Therefore, the reduction of NPP at the coast in HR can be attributed to enhanced eddy quenching. Also Kessouri et al. (2020) found a reduction of nearshore NPP and attributed it to enhanced eddy quenching. However, the reduction in their high-resolution model appears later than in HR. A reason for this delay could be different strengths of CC and CUC which drive eddy formation at the coast. Moreover, Kessouri et al. (2020) used a different atmospheric forcing which also impacts the timing of biological productivity. Nevertheless, the results suggest

that an increase in horizontal resolution enhances eddy quenching and decreases biological productivity at the coast. Albeit, Lagrangian experiments are required to confirm the exact mechanism involved in this reduction.

In the offshore region, NPP is increased in HR by $\sim 6\%$, especially during spring. During this time, biological productivity is highest in the offshore region for both models. The cause of this seasonality can be summarized by two effects (Mahadevan et al., 2012). On the one hand, productivity is low during winter and nutrients can accumulate in the deep mixed layer. On the other hand, the increased solar radiation and decreased buoyancy forcing in spring cause restratification of the surface layer and thereby enhances light exposure time. This leads to an increase in productivity (spring bloom) and consumption of the nutrients (Mahadevan et al., 2012). Submesoscale fronts and associated MLE support restratification and can thereby enhance productivity (Mahadevan et al., 2012) and vertical transport of nutrients (Mahadevan, 2016). Because submesoscale frontogenesis is much better resolved in HR, the increase in NPP in HR during spring is therefore reasonable.

However, there is a discrepancy to results of Kessouri et al. (2020) who found a year-round increase of NPP in the offshore region for their high-resolution model. As mentioned above, offshore productivity is light limited during spring and not driven by coastal processes (Longhurst, 2007). In this regime, submesoscale motions can enhance productivity as soon as they are resolved in the model. In contrast, an enhancement of offshore productivity in a nutrient limited regime (i.e. during summer and autumn) does only work in conjunction with lateral transport of nutrients from the coast (Gruber et al., 2011; Lathuilière et al., 2010). Also Kessouri et al. (2020) ascribe the increase in offshore NPP to a combination of both, an increased nutrient subduction at the coast and a resupply by submesoscale fronts in the offshore region. As discussed, it is very likely that the impact of submesoscale motions on these transport processes is not fully captured in the present study as the nearshore reduction of NPP has not converged at the end of integration in HR. Therefore, the observed discrepancy to results of Kessouri et al. (2020) is presumably be a result of the short integration time in HR.

Overall, the increase in resolution leads to a reduction of NPP at the coast and to an increase in the offshore region. Therefore, the productive band broadens in HR which was stated in hypothesis H3. However, the results should be validated with a longer integration time.

Finally, consequences for mesoscale eddies are discussed. Compared to MR, the EKE of mesoscale eddies in the offshore region is increased by up to 50 % in HR. As described in chapter 1, the inverse energy cascade of mesoscale eddies is driven by the absorption of eddies as small as 17 km and the cascaded energy reaches the mesoscale in late spring or early summer (Capet et al., 2008c; Schubert et al., 2020). This matches the results for HR: small eddies and submesoscale fronts are much better resolved in HR and the increase in EKE is especially strong during early summer. Therefore, the higher EKE in HR can be attributed to a more complete representation of the inverse energy cascade of mesoscale eddies.

By contrast, the density anomaly of mesoscale eddies is impacted in a different way. On the one hand, offshore cyclones reveal a seasonality of the density anomaly in HR which is similar to the trend in EKE. Though, the overall magnitude changes only little and is not intensified as it was hypothesized. On the other hand, offshore anticyclones also obtain a seasonality of the density anomaly in HR which is similar to that of cyclones. However, the anomaly is severely weaker in HR than in MR. During winter, when the weakening is strongest, the density anomaly is reduced by $\sim 40\%$. Therefore, hypothesis H2 has to be modified such that submesoscale fronts mainly weaken the density anomaly in mesoscale anticyclones, whereas cyclones are less affected. This does not contradict the results of Schubert et al. (2019) which motivated this hypothesis, because they only examined the SSH anomaly and not the density anomaly.

The surprisingly strong weakening of offshore anticyclones in HR does not only appear in the reduced density anomaly. Also the increase in EKE associated with anticyclones during winter is, compared to the increase observed for cyclones, very weak. In addition, the enhanced asymmetry between cyclonic and anticyclonic eddies in HR indicates a weakening of anticyclones.

There are several mechanisms which can cause this weakening. First, symmetric instabilities (which drive a forward energy cascade) are pronounced in anticyclones because of the negative vorticity (Thomas et al., 2013). Brannigan et al. (2017) found that instabilities grow in an anticyclone already at 2 km horizontal resolution (similar to HR), whereas a resolution of 0.25 km is required to observe such instabilities in cyclones. Secondly, the detection algorithm for submesoscale fronts revealed that fronts occur more often in anticyclones than in cyclones. The fronts do not only drive a forward energy cascade (D'Asaro et al., 2011), but also cause a positive vertical heat flux from deeper and colder waters to warm waters near the

surface (Klein et al., 2019). This can further undermine the positive temperature anomaly of anticyclones (Frenger et al., 2015). However, the reason for the enhanced presence of submesoscale fronts in anticyclones remains unclear. One explanation might be the negative vorticity which promotes instabilities (Thomas et al., 2013). Another reason could be that the MLD in anticyclones is deeper than in cyclones which favors frontogenesis there.

Considering that submesoscale fronts already appear at the lower limit of horizontal resolution in HR, symmetric instabilities presumably contribute only little to the observed weakening of anticyclones. Instead, we speculate that the heat flux driven by submesoscale fronts is the main cause. Yet, this has to be investigated more systematically in future studies.

Conclusion

There are three important conclusions that can be drawn from the presented results. First, submesoscale fronts shape vertical velocities in the mixed layer. Their omnipresence as well as the strong vertical velocities turns them into important components for upper ocean dynamics. Secondly, submesoscale fronts strongly interact with larger scales, especially with mesoscale eddies. The fronts and MLE fuel an inverse energy cascade, contribute to the seasonality of eddies and also impact their density anomalies. The latter is especially strong in anticyclones and contributes to the dominance of cyclonic polarity. Finally, biological productivity is indeed impacted by the increase in horizontal resolution. Lévy et al. (2018) claimed that the impact of submesoscale fronts on biological productivity is only little because their seasonality is out of phase with biological productivity. However, this should be mitigated for regions where biological productivity is also shaped by mesoscale transport processes. In such regions, to which EBUS and the CCS belong to, productivity is also affected by changes in the mesoscale driven by interactions with submesoscale fronts.

The study demonstrated that submesoscale and mesoscale processes are inextricably linked and that they have to be treated in conjunction with each other. Therefore, numerical models for regional studies should parameterize the discussed effects or deploy a horizontal resolution of $\mathcal{O}(1\text{ km})$, even if the study is not focused on submesoscale processes.

Outlook

The study has several shortcomings which should be addressed in future studies. First, the model should be tuned with special attention to the strength of CC and CUC as well as to a more realistic productivity. Furthermore, the models should be run with a longer integration time to capture also long-term effects. Moreover, it would be beneficial to adjust the atmospheric forcing to a realistic forcing to address the interannual variability in the region. These changes lead to a more realistic representation of the CCS and presumably to a better comparison to observational data.

As mentioned before, the reason for the enhanced presence of submesoscale fronts in anticyclones as well as the exact mechanism for the weakening remain unclear. This should be addressed more systematically in a follow-up study. The developed detection algorithm for submesoscale fronts might be useful for this, but the thresholding step should be improved to reduce the sensitivity to the set of parameters.

Future studies should also consider the interaction of submesoscale motions and coastal filaments. These cold water filaments have sharp density gradients to the surrounding water and play an important role in the lateral export of nutrients (Nagai et al., 2015). Further, submesoscale coherent vortices which encapsulate subsurface water and transport it to offshore regions (Frenger et al., 2018), should be included as well. Also inertial gravity waves which interact with mesoscale motions (Klein et al., 2019) should be considered. Regarding biological productivity, the proposed impacts of submesoscale fronts should be validated in Lagrangian experiments with productive particles. Furthermore, it was shown that submesoscale motions also impact carbon export (Omand et al., 2015; Stukel et al., 2017) and biodiversity (Lévy et al., 2018). These effects can be addressed with the used setup as well. Finally, the applicability of the presented results to other EBUS or other regions should be examined.

Acknowledgements

I would like to thank Dr. Matthias Münnich for his support throughout the project and his constant efforts to set up the submesoscale experiments. Furthermore, I would like to thank Prof. Dr. Nicolas Gruber and Prof. Dr. Norbert Frank for their valuable advice and the opportunity to work on this thesis in the Environmental Physics group at ETH Zurich. I am grateful for the pleasant work atmosphere and the great time I spent with everyone from UP. My special thanks go to Luke and Cara who shared the office with me and answered patiently tons of questions. Finally, I would like to thank my family for their generous support and my girlfriend for her constant encouragement.

Appendices

A Additional Figures

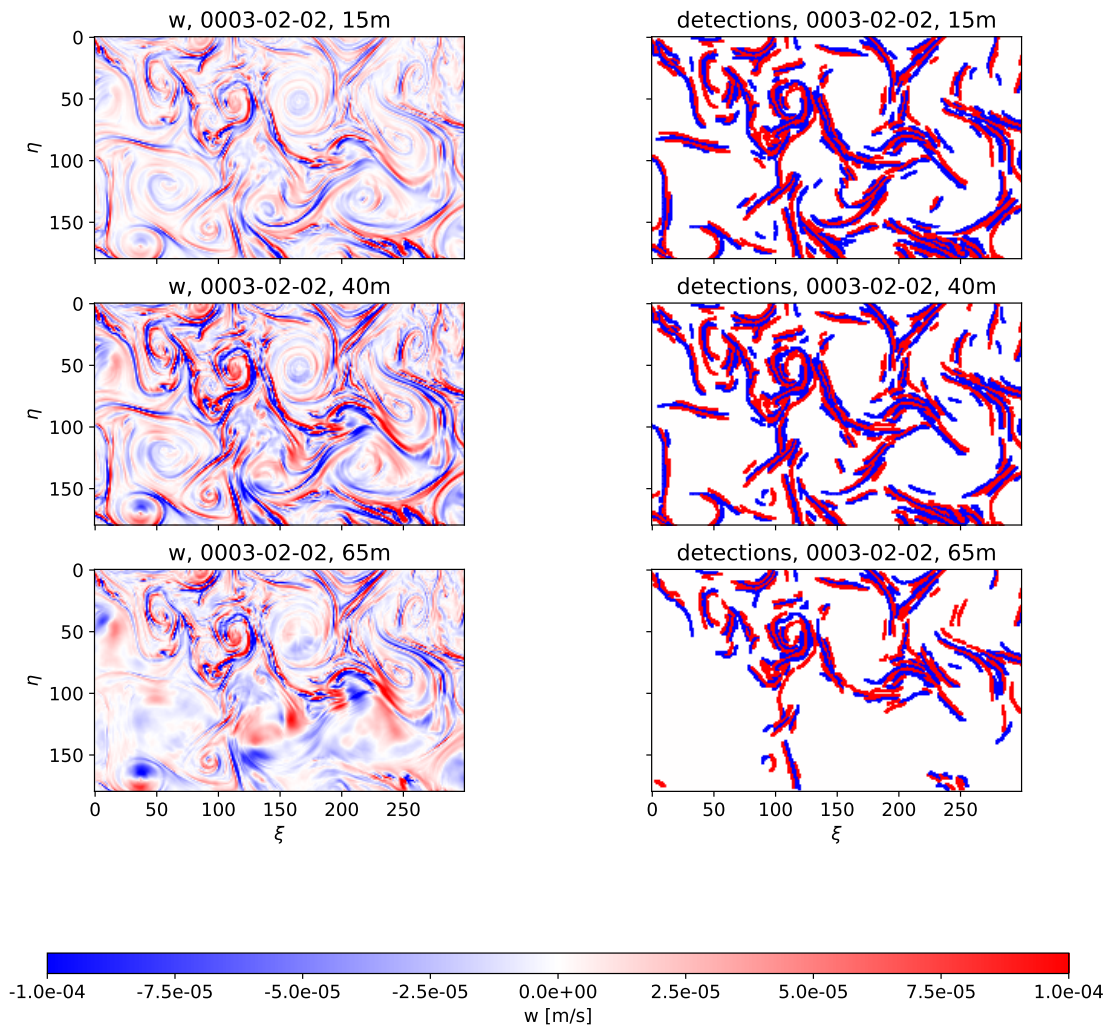


Figure A.1: **Detection results for HR in winter: I.** Data from 0003-02-02 is shown for different depths. The vertical velocity is shown left, the detection results right.

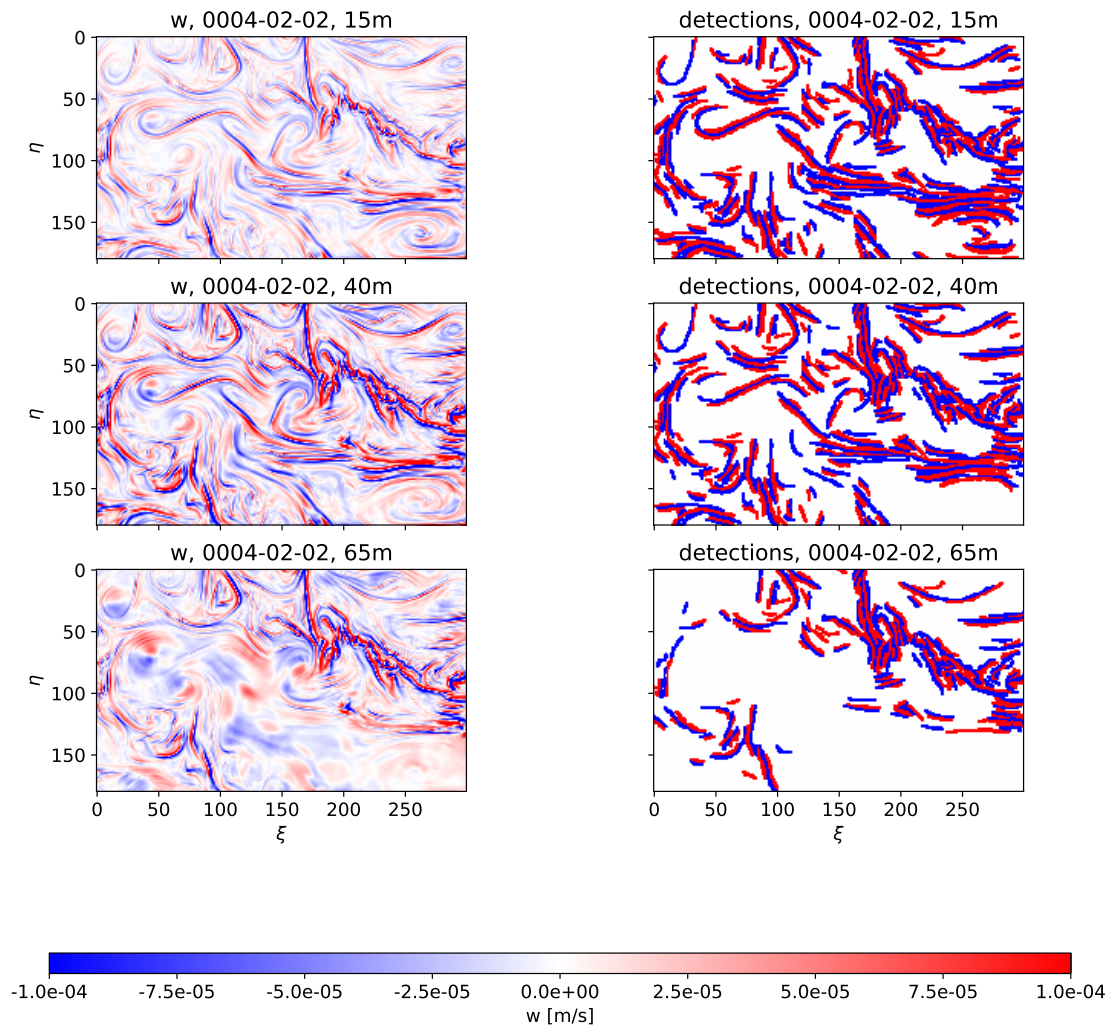


Figure A.2: **Detection results for HR in winter: II.** Data from 0004-02-02 is shown for different depths. The vertical velocity is shown left, the detection results right.

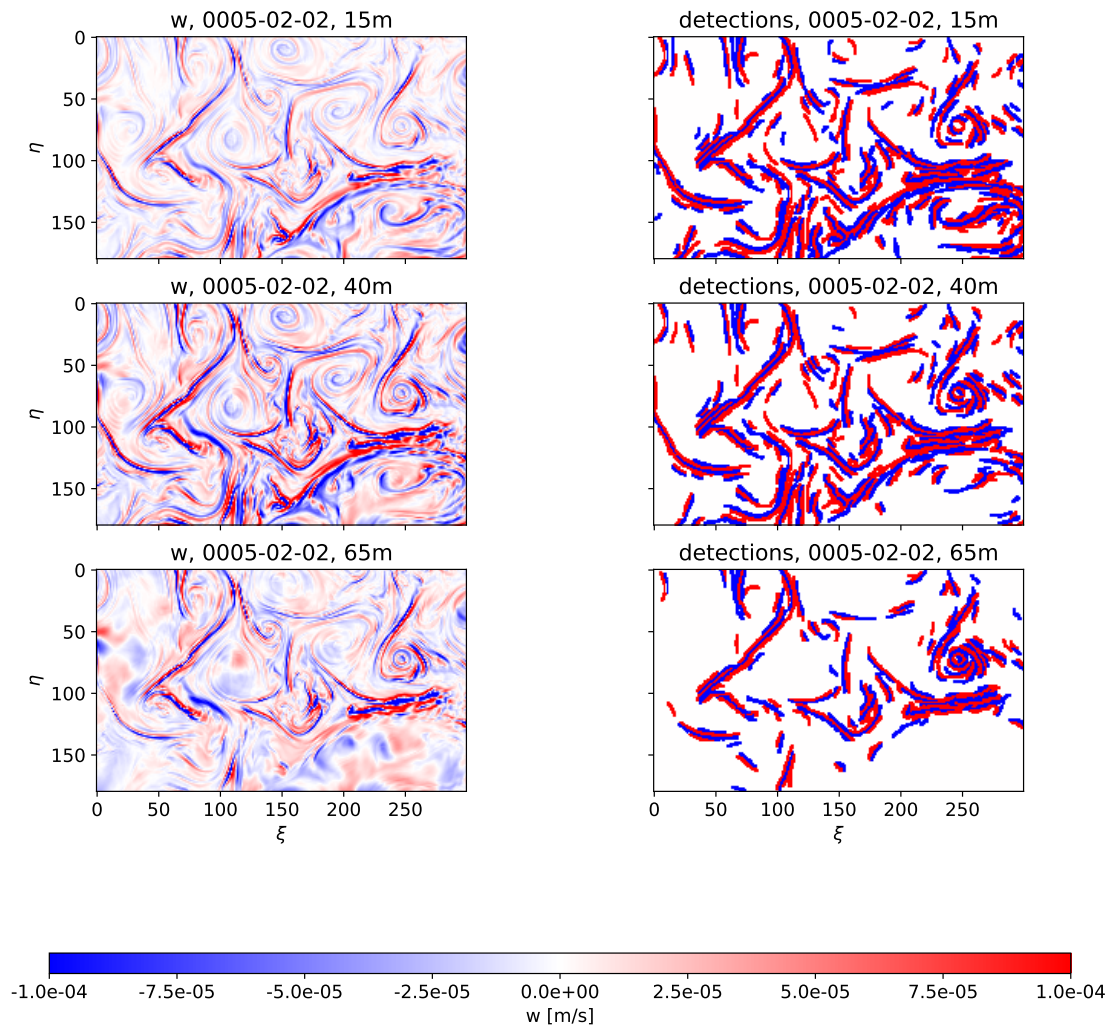


Figure A.3: **Detection results for HR in winter: III.** Data from 0005-02-02 is shown for different depths. The vertical velocity is shown left, the detection results right.

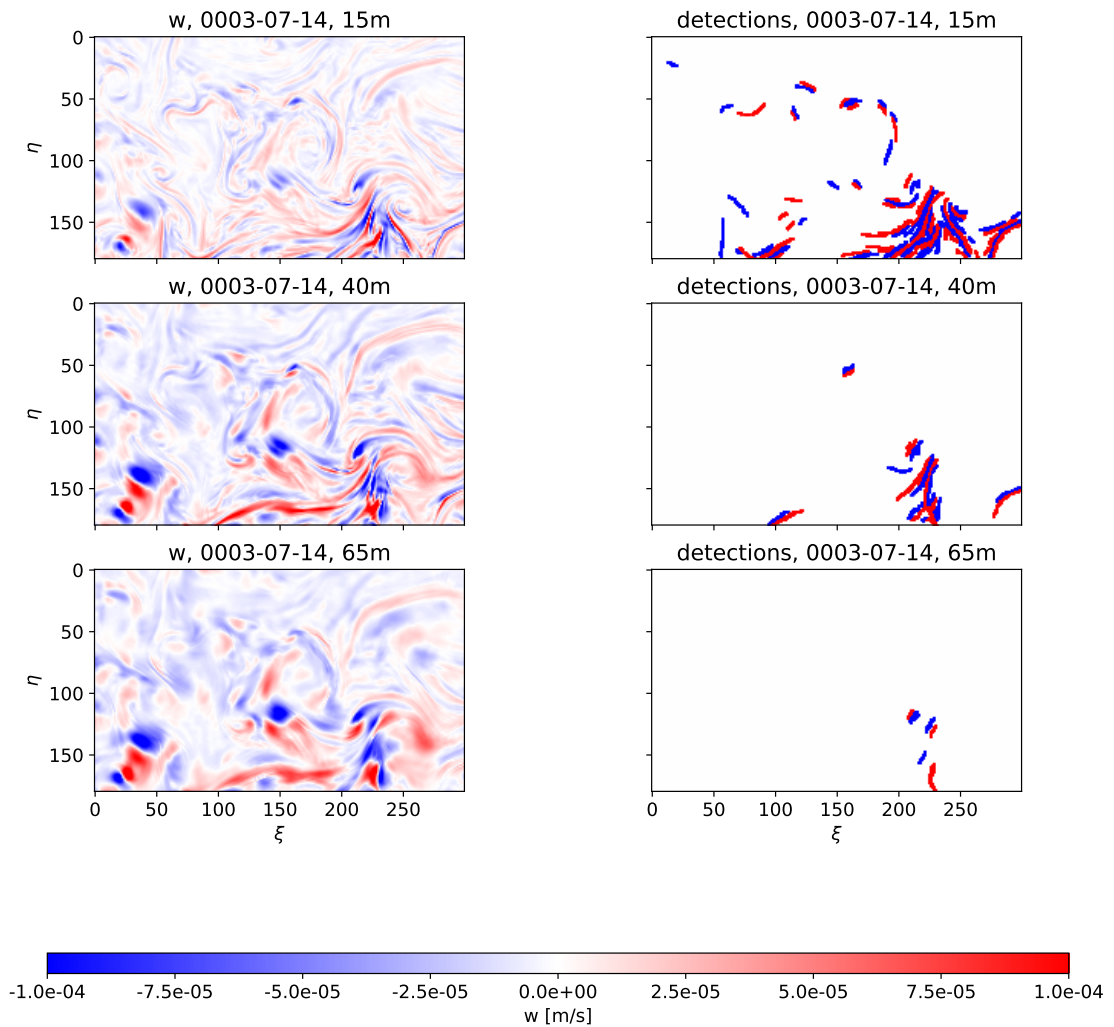


Figure A.4: **Detection results for HR in summer.** Data from 0003-07-14 is shown for different depths. The vertical velocity is shown left, the detection results right.

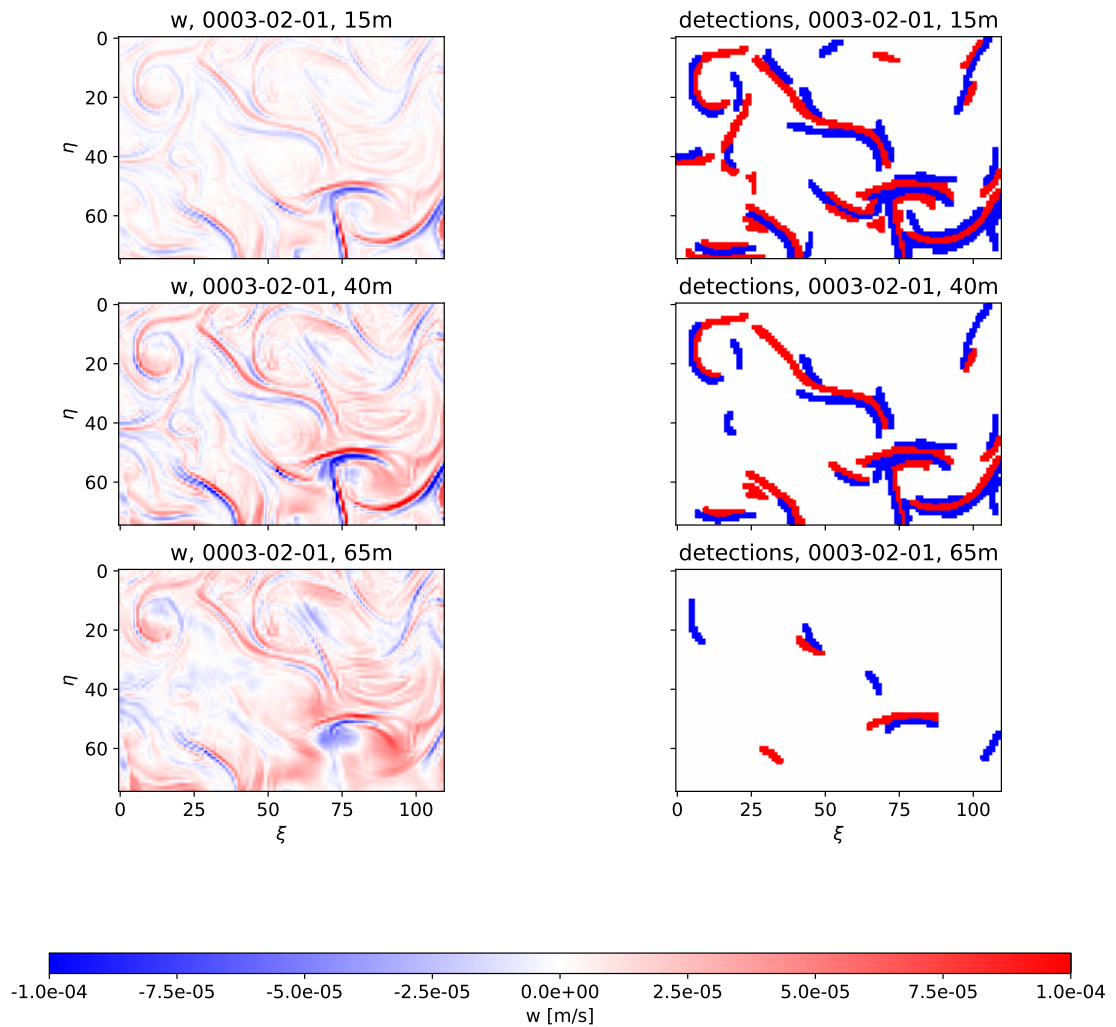


Figure A.5: **Detection results for LR in winter: I.** Data from 0003-02-01 is shown for different depths. The vertical velocity is shown left, the detection results right.

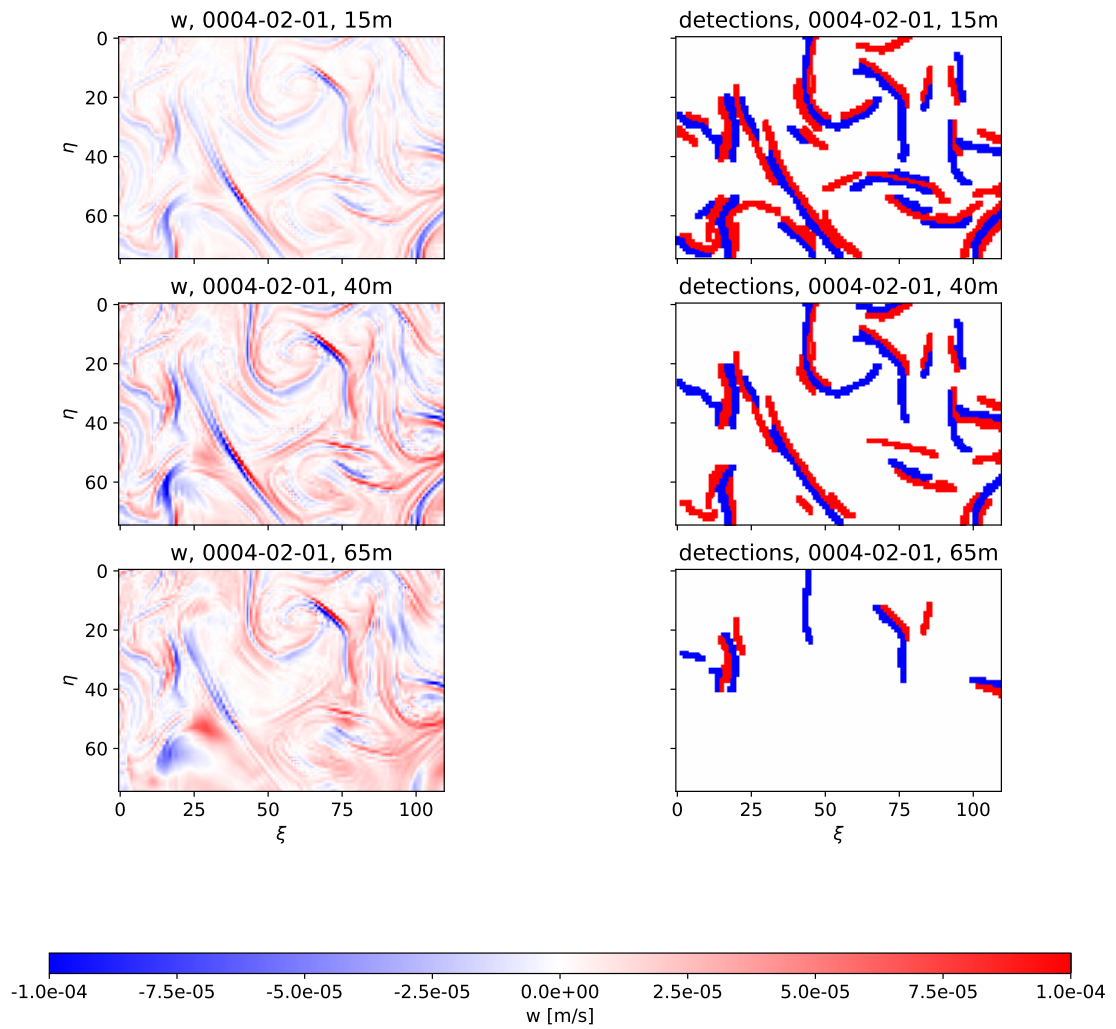


Figure A.6: **Detection results for LR in winter: II.** Data from 0004-02-01 is shown for different depths. The vertical velocity is shown left, the detection results right.

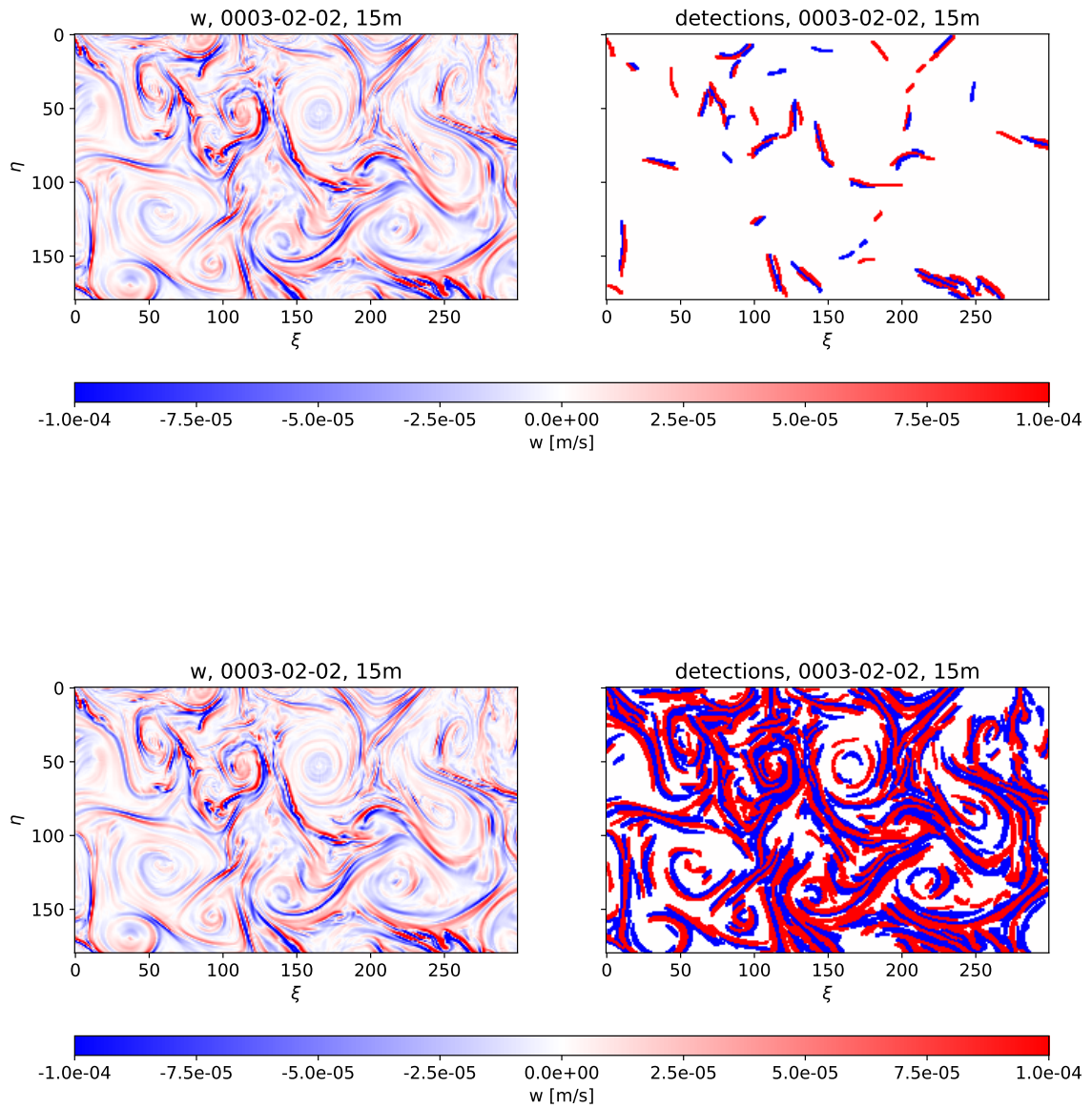


Figure A.7: **Detection results for different σ_{lat} .** Data from 0003-02-01 is shown for $\sigma_{\text{lat}} = 1$ (top) and $\sigma_{\text{lat}} = 4$ (bottom). See Figure A.1 for $\sigma_{\text{t}extlat} = 2$.

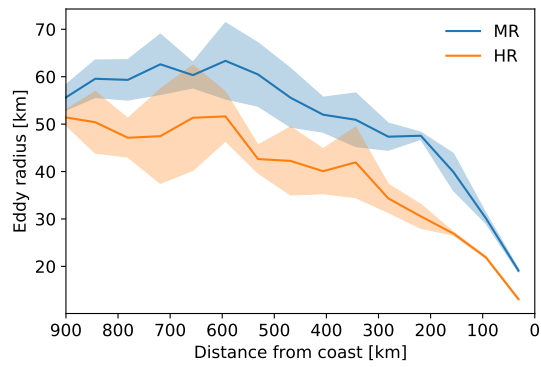


Figure A.8: Eddy radius with distance from coast.

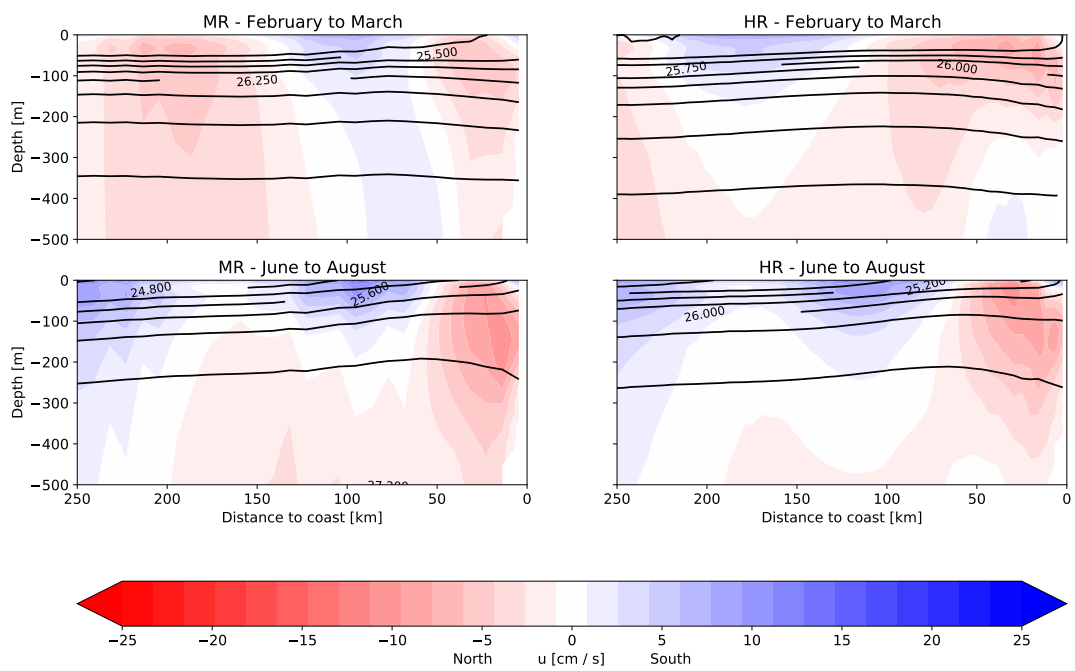


Figure A.9: **California Current and Undercurrent strength.** The horizontal velocity component u (parallel to coast) is shown for winter (top) and summer (bottom). The results for MR are shown left and for HR right. Contours represent isopycnals.

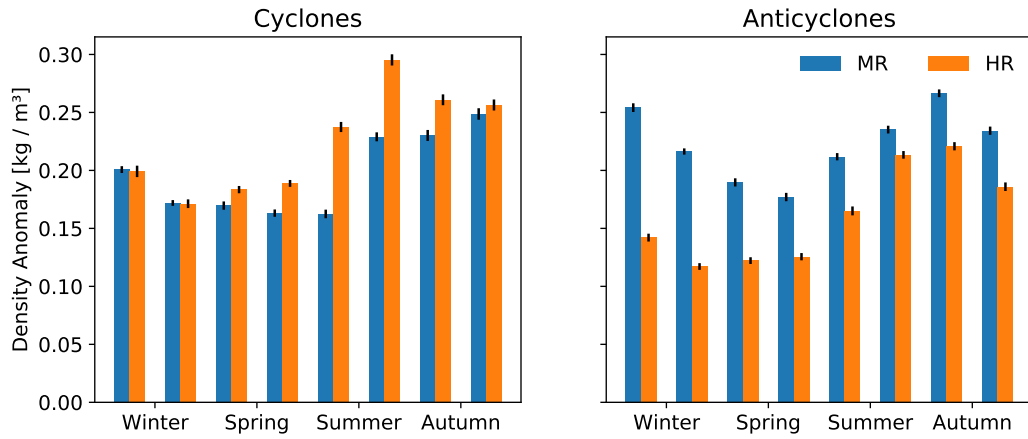


Figure A.10: **Offshore density anomaly (increased depth range)**. Same as Figure 3.5, but averaged from 25m to 200m depth.

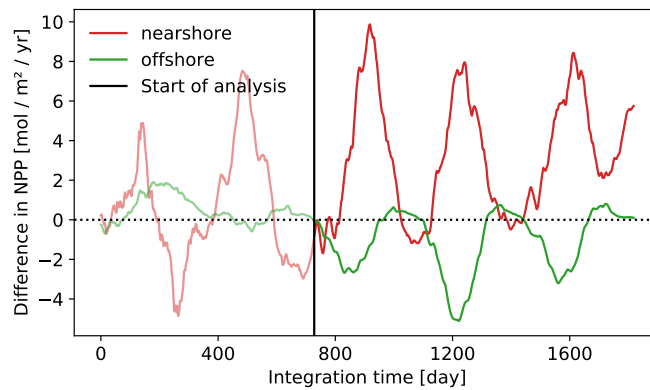


Figure A.11: **Temporal evolution of NPP difference** The difference MR - HR is shown for nearshore region (red) and offshore region (green). The curves were smoothed with a 120d rolling average. The solid black line denotes the start of analysis.

B Lists

List of Figures

2.1	Horizontal grids	7
2.2	Steps of submesoscale front detection algorithm	10
3.1	Distribution of eddy radius	15
3.2	Ratio of cyclonic to anticyclonic tracks	16
3.3	Eddy Kinetic Energy	17
3.4	Vertical structure of temperature anomaly	18
3.5	Offshore density anomaly	19
3.6	Relative increase in offshore EKE	20
3.7	Snapshot of submesoscale fronts in HR	21
3.8	Snapshot of submesoscale fronts in MR	22
3.9	Vertical section of submesoscale fronts	22
3.10	Instabilities in submesoscale fronts	23
3.11	Area covered by submesoscale fronts	24
3.12	Vertical velocity anomaly in HR	25
3.13	Vertical velocity anomaly in MR	26
3.14	Average surface CHL anomaly	28
3.15	Eddy-induced total nitrate flux	29
3.16	Spatial distribution of NPP	30
3.17	Relative change of NPP with distance from coast	30
3.18	Hovmöller diagram of NPP	31
A.1	Detection results for HR in winter: I	40
A.2	Detection results for HR in winter: II	41
A.3	Detection results for HR in winter: III	42
A.4	Detection results for HR in summer	43
A.5	Detection results for LR in winter: I	44
A.6	Detection results for LR in winter: II	45
A.7	Detection results for different σ_{lat}	46
A.8	Relative change of eddy radius with distance from coast	47

A.9 California Current and Undercurrent strength	47
A.10 Offshore density anomaly (increased depth range)	48
A.11 Temporal evolution of NPP difference	48

List of Tables

2.1	Parameters for submesoscale front detection	12
-----	---	----

Bibliography

- Behrenfeld, M. J., & Falkowski, P. G. (1997). Photosynthetic rates derived from satellite-based chlorophyll concentration. *Limnology and Oceanography*, *42*(1), 1–20. <https://doi.org/10.4319/lo.1997.42.1.0001>
- Bentsen, M., Evensen, G., Drange, H., & Jenkins, A. D. (1999). Coordinate transformation on a sphere using conformal mapping. *Monthly Weather Review*, *127*(12), 2733–2740.
- Boccaletti, G., Ferrari, R., & Fox-Kemper, B. (2007). Mixed layer instabilities and restratification. *Journal of Physical Oceanography*, *37*(9), 2228–2250. <https://doi.org/10.1175/JPO3101.1>
- Bograd, S. J., & Lynn, R. J. (2001). Physical-biological coupling in the California Current during the 1997-99 El Niño-La Niña Cycle. *Geophysical Research Letters*, *28*(2), 275–278. <https://doi.org/10.1029/2000GL012047>
- Brannigan, L., Marshall, D. P., Garabato, A. C., Nurser, A. J., & Kaiser, J. (2017). Submesoscale instabilities in mesoscale eddies. *Journal of Physical Oceanography*, *47*(12), 3061–3085. <https://doi.org/10.1175/JPO-D-16-0178.1>
- Callies, J., Ferrari, R., Klymak, J. M., & Gula, J. (2015). Seasonality in submesoscale turbulence. *Nature Communications*, *6*(1), 1–8. <https://doi.org/10.1038/ncomms7862>
- Capet, X., McWilliams, J. C., Molemaker, M. J., & Shchepetkin, A. F. (2008a). Mesoscale to submesoscale transition in the California Current system. Part I: Flow structure, eddy flux, and observational tests. *Journal of Physical Oceanography*, *38*(1), 29–43. <https://doi.org/10.1175/2007JPO3671.1>
- Capet, X., McWilliams, J. C., Molemaker, M. J., & Shchepetkin, A. F. (2008b). Mesoscale to submesoscale transition in the California Current system. Part II: Frontal processes. *Journal of Physical Oceanography*, *38*(1), 44–64. <https://doi.org/10.1175/2007JPO3672.1>

- Capet, X., McWilliams, J. C., Molemaker, M. J., & Shchepetkin, A. F. (2008c). Mesoscale to submesoscale transition in the California current system. Part III: Energy balance and flux. *Journal of Physical Oceanography*, *38*(10), 2256–2269. <https://doi.org/10.1175/2008JPO3810.1>
- Carr, M. E. (2001). Estimation of potential productivity in Eastern Boundary Currents using remote sensing. *Deep-Sea Research Part II: Topical Studies in Oceanography*, *49*(1-3), 59–80. [https://doi.org/10.1016/S0967-0645\(01\)00094-7](https://doi.org/10.1016/S0967-0645(01)00094-7)
- Chaigneau, A., Eldin, G., & Dewitte, B. (2009). Eddy activity in the four major upwelling systems from satellite altimetry (1992-2007). *Progress in Oceanography*, *83*(1-4), 117–123. <https://doi.org/10.1016/j.pocean.2009.07.012>
- Chavez, F. P., & Messié, M. (2009). A comparison of Eastern Boundary Upwelling Ecosystems. *Progress in Oceanography*, *83*(1-4), 80–96. <https://doi.org/10.1016/j.pocean.2009.07.032>
- Checkley, D. M., & Barth, J. A. (2009). Patterns and processes in the California Current System. *Progress in Oceanography*, *83*(1-4), 49–64. <https://doi.org/10.1016/j.pocean.2009.07.028>
- Chelton, D. B., Gaube, P., Schlax, M. G., Early, J. J., & Samelson, R. M. (2011). The influence of nonlinear mesoscale eddies on near-surface oceanic chlorophyll. *Science*, *334*(6054), 328–332. <https://doi.org/10.1126/science.1208897>
- Chelton, D. B., Schlax, M. G., & Samelson, R. M. (2011). Global observations of nonlinear mesoscale eddies. *Progress in Oceanography*, *91*(2), 167–216. <https://doi.org/10.1016/j.pocean.2011.01.002>
- D’Asaro, E., Lee, C., Rainville, L., Harcourt, R., & Thomas, L. (2011). Enhanced turbulence and energy dissipation at ocean fronts. *Science*, *332*(6027), 318–322. <https://doi.org/10.1126/science.1201515>
- Deutsch, C., Frenzel, H., McWilliams, J., Renault, L., Kessouri, F., Howard, E., Liang, J.-H., Bianchi, D., & Yang, S. (2020). Biogeochemical variability in the California Current System. *bioRxiv*, 2020.02.10.942565. <https://doi.org/10.1101/2020.02.10.942565>
- Ducet, N., Le Traon, P. Y., & Reverdin, G. (2000). Global high-resolution mapping of ocean circulation from TOPEX/Poseidon and ERS-1 and -2. *Journal of Geophysical Research: Oceans*, *105*(C8), 19477–19498. <https://doi.org/10.1029/2000jc900063>
- Faghmous, J. H., Frenger, I., Yao, Y., Warmka, R., Lindell, A., & Kumar, V. (2015). A daily global mesoscale ocean eddy dataset from satellite altimetry. *Scientific Data*, *2*(1), 1–16. <https://doi.org/10.1038/sdata.2015.28>

- Falkowski, P. G., Ziemann, D., Kolber, Z., & Bienfang, P. K. (1991). Role of eddy pumping in enhancing primary production in the ocean. *Nature*, *352*(6330), 55–58. <https://doi.org/10.1038/352055a0>
- Flierl, G. R. (1981). Particle Motions in Large-Amplitude Wave Fields. *Geophysical & Astrophysical Fluid Dynamics*, *18*(1-2), 39–74. <https://doi.org/10.1080/03091928108208773>
- Fox-Kemper, B., Adcroft, A., Böning, C. W., Chassignet, E. P., Curchitser, E., Danabasoglu, G., Eden, C., England, M. H., Gerdes, R., Greatbatch, R. J., Griffies, S. M., Hallberg, R. W., Hanert, E., Heimbach, P., Hewitt, H. T., Hill, C. N., Komuro, Y., Legg, S., Le Sommer, J., ... Yeager, S. G. (2019). Challenges and prospects in ocean circulation models. *Frontiers in Marine Science*, *6*, 65. <https://doi.org/10.3389/fmars.2019.00065>
- Fox-Kemper, B., Ferrari, R., & Hallberg, R. (2008). Parameterization of mixed layer eddies. Part I: Theory and diagnosis. *Journal of Physical Oceanography*, *38*(6), 1145–1165. <https://doi.org/10.1175/2007JPO3792.1>
- Freilich, M. A., & Mahadevan, A. (2019). Decomposition of vertical velocity for nutrient transport in the upper ocean. *Journal of Physical Oceanography*, *49*(6), 1561–1575. <https://doi.org/10.1175/JPO-D-19-0002.1>
- Frenger, I., Münnich, M., Gruber, N., & Knutti, R. (2015). Southern Ocean eddy phenomenology. *Journal of Geophysical Research: Oceans*, *120*(11), 7413–7449. <https://doi.org/10.1002/2015JC011047>
- Frenger, I., Bianchi, D., Stührenberg, C., Oschlies, A., Dunne, J., Deutsch, C., Galbraith, E., & Schütte, F. (2018). Biogeochemical Role of Subsurface Coherent Eddies in the Ocean: Tracer Cannonballs, Hypoxic Storms, and Microbial Stewpots? *Global Biogeochemical Cycles*, *32*(2), 226–249. <https://doi.org/10.1002/2017GB005743>
- Friedrichs, M. A., Carr, M. E., Barber, R. T., Scardi, M., Antoine, D., Armstrong, R. A., Asanuma, I., Behrenfeld, M. J., Buitenhuis, E. T., Chai, F., Christian, J. R., Ciotti, A. M., Doney, S. C., Dowell, M., Dunne, J., Gentili, B., Gregg, W., Hoepffner, N., Ishizaka, J., ... Winguth, A. (2009). Assessing the uncertainties of model estimates of primary productivity in the tropical Pacific Ocean. *Journal of Marine Systems*, *76*(1-2), 113–133. <https://doi.org/10.1016/j.jmarsys.2008.05.010>
- Frischknecht, M., Münnich, M., & Gruber, N. (2015). Remote versus local influence of ENSO on the California Current System. *Journal of Geophysical Research: Oceans*, *120*(2), 1353–1374. <https://doi.org/10.1002/2014JC010531>

- Frischknecht, M., Münnich, M., & Gruber, N. (2018). Origin, Transformation, and Fate: The Three-Dimensional Biological Pump in the California Current System. *Journal of Geophysical Research: Oceans*, *123*(11), 7939–7962. <https://doi.org/10.1029/2018JC013934>
- Frischknecht, M., Münnich, M., & Gruber, N. (2017). Local atmospheric forcing driving an unexpected California Current System response during the 2015–2016 El Niño. *Geophysical Research Letters*, *44*(1), 304–311. <https://doi.org/10.1002/2016GL071316>
- Gaube, P., Chelton, D. B., Samelson, R. M., Schlax, M. G., & O’Neill, L. W. (2015). Satellite observations of mesoscale eddy-induced Ekman pumping. *Journal of Physical Oceanography*, *45*(1), 104–132. <https://doi.org/10.1175/JPO-D-14-0032.1>
- Gaube, P., McGillicuddy, D. J., Chelton, D. B., Behrenfeld, M. J., & Strutton, P. G. (2014). Regional variations in the influence of mesoscale eddies on near-surface chlorophyll. *Journal of Geophysical Research: Oceans*, *119*(12), 8195–8220. <https://doi.org/10.1002/2014JC010111>
- Gruber, N., Lachkar, Z., Frenzel, H., Marchesiello, P., Münnich, M., McWilliams, J. C., Nagai, T., & Plattner, G. K. (2011). Eddy-induced reduction of biological production in eastern boundary upwelling systems. *Nature Geoscience*, *4*(11), 787–792. <https://doi.org/10.1038/ngeo1273>
- Haine, T. W., & Marshall, J. (1998). Gravitational, symmetric, and baroclinic instability of the ocean mixed layer. *Journal of Physical Oceanography*, *28*(4), 634–658. [https://doi.org/10.1175/1520-0485\(1998\)028<0634:GSABIO>2.0.CO;2](https://doi.org/10.1175/1520-0485(1998)028<0634:GSABIO>2.0.CO;2)
- Hersbach, H., Bell, B., Berrisford, P., Hirahara, S., Horányi, A., Muñoz-Sabater, J., Nicolas, J., Peubey, C., Radu, R., Schepers, D., Simmons, A., Soci, C., Abdalla, S., Abellan, X., Balsamo, G., Bechtold, P., Biavati, G., Bidlot, J., Bonavita, M., ... Thépaut, J.-N. (2020). The ERA5 global reanalysis. *Quarterly Journal of the Royal Meteorological Society*, *146*(730). <https://doi.org/10.1002/qj.3803>
- Huyer, A. (1983). Coastal upwelling in the California current system. *Progress in Oceanography*, *12*(3), 259–284. [https://doi.org/10.1016/0079-6611\(83\)90010-1](https://doi.org/10.1016/0079-6611(83)90010-1)
- Huyer, A., Kosro, P. M., Fleischbein, J., Ramp, S. R., Stanton, T., Washburn, L., Chavez, F. P., Cowles, T. J., Pierce, S. D., & Smith, R. L. (1991). Currents and water masses of the Coastal Transition Zone off northern California, June to August 1988. *Journal of Geophysical Research: Oceans*, *96*(C8), 14809–

14831. [https://doi.org/10.1029/91JC00641@10.1002/\(ISSN\)2169-9291.CTZ1](https://doi.org/10.1029/91JC00641@10.1002/(ISSN)2169-9291.CTZ1)
- Kahru, M., Kudela, R., Manzano-Sarabia, M., & Mitchell, B. G. (2009). Trends in primary production in the California Current detected with satellite data. *Journal of Geophysical Research*, *114*(C2), C02004. <https://doi.org/10.1029/2008JC004979>
- Kelly, K. A., Beardsley, R. C., Limeburner, R., Brink, K. H., Paduan, J. D., & Chereskin, T. K. (1998). Variability of the near-surface eddy kinetic energy in the California current based on altimetric, drifter, and moored current data. *Journal of Geophysical Research: Oceans*, *103*(3336), 13067–13083. <https://doi.org/10.1029/97jc03760>
- Kessouri, F., Bianchi, D., Renault, L., McWilliams, J. C., Frenzel, H., & Deutsch, C. (2020). Submesoscale currents modulate the seasonal cycle of nutrients and productivity in the California Current System. *Global Biogeochemical Cycles*, *34*(10). <https://doi.org/10.1029/2020gb006578>
- Klein, P., Lapeyre, G., Siegelman, L., Qiu, B., Fu, L.-L., Torres, H., Su, Z., Menemenlis, D., & Le Gentil, S. (2019). Ocean-Scale Interactions From Space. *Earth and Space Science*, *6*(5), 795–817. <https://doi.org/10.1029/2018EA000492>
- Kurian, J., Colas, F., Capet, X., McWilliams, J. C., & Chelton, D. B. (2011). Eddy properties in the California Current System. *Journal of Geophysical Research: Oceans*, *116*(8). <https://doi.org/10.1029/2010JC006895>
- Lapeyre, G., & Klein, P. (2006). Impact of the small-scale elongated filaments on the oceanic vertical pump. *Journal of Marine Research*, *64*(6), 835–851. <https://doi.org/10.1357/002224006779698369>
- Large, W. G., McWilliams, J. C., & Doney, S. C. (1994). Oceanic vertical mixing: A review and a model with a nonlocal boundary layer parameterization. *Reviews of Geophysics*, *32*(4), 363–403. [https://doi.org/https://doi.org/10.1029/94RG01872](https://doi.org/10.1029/94RG01872)
- Lathuilière, C., Echevin, V., Lévy, M., & Madec, G. (2010). On the role of the mesoscale circulation on an idealized coastal upwelling ecosystem. *Journal of Geophysical Research*, *115*(C9), C09018. <https://doi.org/10.1029/2009JC005827>
- Lévy, M., Iovino, D., Resplandy, L., Klein, P., Madec, G., Tréguier, A. M., Masson, S., & Takahashi, K. (2012). Large-scale impacts of submesoscale dynamics on phytoplankton: Local and remote effects. *Ocean Modelling*, *43-44*, 77–93. <https://doi.org/10.1016/j.ocemod.2011.12.003>

- Lévy, M., Ferrari, R., Franks, P. J., Martin, A. P., & Rivière, P. (2012). Bringing physics to life at the submesoscale. *Geophysical Research Letters*, *39*(14). <https://doi.org/10.1029/2012GL052756>
- Lévy, M., Franks, P. J., & Smith, K. S. (2018). The role of submesoscale currents in structuring marine ecosystems. *Nature Communications*, *9*(1), 1–16. <https://doi.org/10.1038/s41467-018-07059-3>
- Lévy, M., Klein, P., & Treguier, A.-M. (2001). *Impact of sub-mesoscale physics on production and subduction of phytoplankton in an oligotrophic regime* (tech. rep. No. 4). Yale University.
- Longhurst, A. R. (2007). THE PACIFIC OCEAN. *Ecological geography of the sea* (pp. 399–403). Elsevier. <https://doi.org/10.1016/b978-012455521-1/50012-7>
- Lovecchio, E., Gruber, N., & Münnich, M. (2018). Mesoscale contribution to the long-range offshore transport of organic carbon from the Canary Upwelling System to the open North Atlantic. *Biogeosciences*, *15*(16), 5061–5091. <https://doi.org/10.5194/bg-15-5061-2018>
- Mahadevan, A. (2016). The Impact of Submesoscale Physics on Primary Productivity of Plankton. *Annual Review of Marine Science*, *8*(1), 161–184. <https://doi.org/10.1146/annurev-marine-010814-015912>
- Mahadevan, A., D’Asaro, E., Lee, C., & Perry, M. J. (2012). Eddy-driven stratification initiates North Atlantic spring phytoplankton blooms. *Science*, *336*(6090), 54–58. <https://doi.org/10.1126/science.1218740>
- Mahadevan, A., & Tandon, A. (2006). An analysis of mechanisms for submesoscale vertical motion at ocean fronts. *Ocean Modelling*, *14*(3-4), 241–256. <https://doi.org/10.1016/j.ocemod.2006.05.006>
- Martin, A. P., & Richards, K. J. (2001). Mechanisms for vertical nutrient transport within a North Atlantic mesoscale eddy. *Deep-Sea Research Part II: Topical Studies in Oceanography*, *48*(4-5), 757–773. [https://doi.org/10.1016/S0967-0645\(00\)00096-5](https://doi.org/10.1016/S0967-0645(00)00096-5)
- McCreary, J. P., Kundu, P. K., & Chao, S.-Y. (1987). On the dynamics of the California Current system. *Journal of Marine Research*, *45*(1). <https://doi.org/10.1357/002224087788400945>
- McGillicuddy, D. J. (2016). Mechanisms of Physical-Biological-Biogeochemical Interaction at the Oceanic Mesoscale. *Annual Review of Marine Science*, *8*(1), 125–159. <https://doi.org/10.1146/annurev-marine-010814-015606>
- McGillicuddy, D. J., Ledwell, J. R., & Anderson, L. A. (2008). Response to comment on “eddy/wind interactions stimulate extraordinary mid-ocean plank-

- ton blooms". *Science*, *320*(5875), 448–448. <https://doi.org/10.1126/science.1148974>
- McWilliams, J. C. (1985). Submesoscale, coherent vortices in the ocean. *Reviews of Geophysics*, *23*(2), 165–182. <https://doi.org/https://doi.org/10.1029/RG023i002p00165>
- McWilliams, J. C. (2008). The nature and consequences of oceanic eddies. *Geophysical monograph series* (pp. 5–15). Blackwell Publishing Ltd. <https://doi.org/10.1029/177GM03>
- McWilliams, J. C. (2016). Submesoscale currents in the ocean. *Proceedings of the Royal Society A: Mathematical, Physical and Engineering Sciences*, *472*(2189), 20160117. <https://doi.org/10.1098/rspa.2016.0117>
- McWilliams, J. C. (2019). A survey of submesoscale currents. *Geoscience Letters*, *6*(1), 1–15. <https://doi.org/10.1186/s40562-019-0133-3>
- McWilliams, J. C., Molemaker, M. J., & Yavneh, I. (2004). Ageostrophic, anticyclonic instability of a geostrophic, barotropic boundary current. *Physics of Fluids*, *16*(10), 3720–3725. <https://doi.org/10.1063/1.1785132>
- Mensa, J. A., Garraffo, Z., Griffa, A., Özgökmen, T. M., Haza, A., & Veneziani, M. (2013). Seasonality of the submesoscale dynamics in the Gulf Stream region. *Ocean Dynamics*, *63*(8), 923–941. <https://doi.org/10.1007/s10236-013-0633-1>
- Moore, J. K., Lindsay, K., Doney, S. C., Long, M. C., & Misumi, K. (2013). Marine ecosystem dynamics and biogeochemical cycling in the community earth system model [CESM1(BGC)]: Comparison of the 1990s with the 2090s under the RCP4.5 and RCP8.5 scenarios. *Journal of Climate*, *26*(23), 9291–9312. <https://doi.org/10.1175/JCLI-D-12-00566.1>
- Nagai, T., Gruber, N., Frenzel, H., Lachkar, Z., McWilliams, J. C., & Plattner, G.-K. (2015). Dominant role of eddies and filaments in the offshore transport of carbon and nutrients in the California Current System. *Journal of Geophysical Research: Oceans*, *120*(8), 5318–5341. <https://doi.org/10.1002/2015JC010889>
- Omand, M. M., D’Asaro, E. A., Lee, C. M., Perry, M. J., Briggs, N., Cetinić, I., & Mahadevan, A. (2015). Eddy-driven subduction exports particulate organic carbon from the spring bloom. *Science*, *348*(6231), 222–225. <https://doi.org/10.1126/science.1260062>
- Renault, L., Deutsch, C., McWilliams, J. C., Frenzel, H., Liang, J. H., & Colas, F. (2016). Partial decoupling of primary productivity from upwelling in the

- California Current system. *Nature Geoscience*, 9(7), 505–508. <https://doi.org/10.1038/ngeo2722>
- Renault, L., McWilliams, J., Jousse, A., Deutsch, C., Frenzel, H., Kessouri, F., & Chen, R. (2020). The Physical Structure and Behavior of the California Current System. *bioRxiv*, 2020.02.10.942730. <https://doi.org/10.1101/2020.02.10.942730>
- Rieck, J. K. (2019). *The Nature and Variability of Eddy Kinetic Energy in an Ocean General Circulation Model With a Focus on the South Pacific Subtropical Gyre and the Labrador Sea* (Doctoral dissertation). Christians-Albrecht-Universität. Kiel.
- Rossi, V., López, C., Sudre, J., Hernández-García, E., & Garçon, V. (2008). Comparative study of mixing and biological activity of the Benguela and Canary upwelling systems. *Geophysical Research Letters*, 35(11), L11602. <https://doi.org/10.1029/2008GL033610>
- Rudnick, D. L., Zaba, K. D., Todd, R. E., & Davis, R. E. (2017). A climatology of the California Current System from a network of underwater gliders. *Progress in Oceanography*, 154, 64–106. <https://doi.org/10.1016/j.pocean.2017.03.002>
- Sasaki, H., Klein, P., Qiu, B., & Sasai, Y. (2014). Impact of oceanic-scale interactions on the seasonal modulation of ocean dynamics by the atmosphere. *Nature Communications*, 5(1), 1–8. <https://doi.org/10.1038/ncomms6636>
- Schubert, R., Schwarzkopf, F. U., Baschek, B., & Biastoch, A. (2019). Submesoscale Impacts on Mesoscale Agulhas Dynamics. *Journal of Advances in Modeling Earth Systems*, 11(8), 2745–2767. <https://doi.org/10.1029/2019MS001724>
- Schubert, R., Gula, J., Greatbatch, R. J., Baschek, B., & Biastoch, A. (2020). The submesoscale kinetic energy cascade: Mesoscale absorption of submesoscale mixed layer eddies and frontal downscale fluxes. *Journal of Physical Oceanography*, 50(9), 2573–2589. <https://doi.org/10.1175/JPO-D-19-0311.1>
- Shchepetkin, A. F., & McWilliams, J. C. (2005). The regional oceanic modeling system (ROMS): A split-explicit, free-surface, topography-following-coordinate oceanic model. *Ocean Modelling*, 9(4), 347–404. <https://doi.org/10.1016/j.ocemod.2004.08.002>
- Shu, C.-W. (1998). Essentially non-oscillatory and weighted essentially non-oscillatory schemes for hyperbolic conservation laws. Springer, Berlin, Heidelberg. <https://doi.org/10.1007/bfb0096355>
- Song, Y., & Haidvogel, D. (1994). A semi-implicit ocean circulation model using a generalized topography-following coordinate system. *Journal of Computational Physics*, 115(1), 228–244. <https://doi.org/10.1006/jcph.1994.1189>

- Stern, M. E. (1965). Interaction of a uniform wind stress with a geostrophic vortex. *Deep-Sea Research and Oceanographic Abstracts*, 12(3), 355–367. [https://doi.org/10.1016/0011-7471\(65\)90007-0](https://doi.org/10.1016/0011-7471(65)90007-0)
- Stukel, M. R., Aluwihare, L. I., Barbeau, K. A., Chekalyuk, A. M., Goericke, R., Miller, A. J., Ohman, M. D., Ruacho, A., Song, H., Stephens, B. M., & Landry, M. R. (2017). Mesoscale ocean fronts enhance carbon export due to gravitational sinking and subduction. *Proceedings of the National Academy of Sciences of the United States of America*, 114(6), 1252–1257. <https://doi.org/10.1073/pnas.1609435114>
- Thomas, L. N., & Lee, C. M. (2005). Intensification of ocean fronts by down-front winds. *Journal of Physical Oceanography*, 35(6), 1086–1102. <https://doi.org/10.1175/JPO2737.1>
- Thomas, L. N., Tandon, A., & Mahadevan, A. (2008). Submesoscale processes and dynamics. *Geophysical monograph series* (pp. 17–38). Blackwell Publishing Ltd. <https://doi.org/10.1029/177GM04>
- Thomas, L. N., Taylor, J. R., Ferrari, R., & Joyce, T. M. (2013). Symmetric instability in the Gulf Stream. *Deep-Sea Research Part II: Topical Studies in Oceanography*, 91, 96–110. <https://doi.org/10.1016/j.dsr2.2013.02.025>
- Tulloch, R., Marshall, J., Hill, C., & Smith, K. S. (2011). Scales, Growth rates, and spectral fluxes of baroclinic instability in the ocean. *Journal of Physical Oceanography*, 41(6), 1057–1076. <https://doi.org/10.1175/2011JPO4404.1>
- Vandemeulebrouck, R., & Münnich, M. (2020). *Implementation and analysis of a WENO scheme* (Master's thesis). Faculty of Maths, Computational Science. Lusanne.
- Vic, C., Gula, J., Roulet, G., & Pradillon, F. (2018). Dispersion of deep-sea hydrothermal vent effluents and larvae by submesoscale and tidal currents. *Deep-Sea Research Part I: Oceanographic Research Papers*, 133, 1–18. <https://doi.org/10.1016/j.dsr.2018.01.001>
- Whitt, D. B., Lévy, M., & Taylor, J. R. (2019). Submesoscales Enhance Storm-Driven Vertical Mixing of Nutrients: Insights From a Biogeochemical Large Eddy Simulation. *Journal of Geophysical Research: Oceans*, 124(11), 8140–8165. <https://doi.org/10.1029/2019JC015370>
- Whitt, D. B., & Taylor, J. R. (2017). Energetic submesoscales maintain strong mixed layer stratification during an autumn storm. *Journal of Physical Oceanography*, 47(10), 2419–2427. <https://doi.org/10.1175/JPO-D-17-0130.1>

Selbstständigkeitserklärung

Ich versichere, dass ich diese Arbeit selbstständig verfasst habe und keine anderen als die angegebenen Quellen und Hilfsmittel benutzt habe.

Zürich, den 18.12.2020

.....*M. Simon*.....